Numerical assessment of the seismic vulnerability of the historical earthen remains of the Mansourah enclosure (Tlemcen, Algeria): influence of geometry and identification of critical damage zones

Hanini Walid, Boumechra Nadir
EOLE research laboratory, Faculty of Technology, University of Tlemcen, Algeria
haniniwalid@gmail.com, https://orcid.org/0009-0008-2462-1596
n_boumechra@yahoo.fr, https://orcid.org/0000-0001-9301-4003

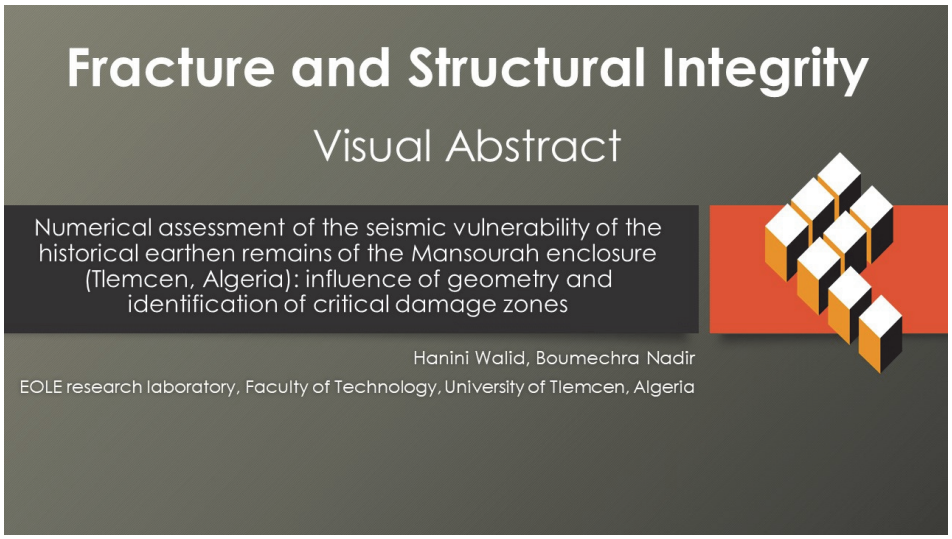

Citation: Hanini, W., Boumechra, N., Numerical assessment of the seismic vulnerability of the historical earthen remains of the Mansourah enclosure (Tlemcen, Algeria): influence of geometry and identification of critical damage zones, Fracture and Structural Integrity, 76 (2026) 183-211.

Received: 22.11.2025
Accepted: 30.01.2026
Published: 15.02.2026
Issue: 04.2026

KEYWORDS. Rammed Earth, Nonlinear behavior, critical zones, damage, Seismic vulnerability, Drucker–Prager criterion.

INTRODUCTION

Nowadays, more than half of the world's population lives in earthen buildings. Many of these buildings are located in France, Germany, Spain, North Africa, Australia, North and South America, and Asia, particularly China, Japan, and some other regions [1].

Rammed Earth (RE) is a basic building material that has been widely used in many regions around the world for several centuries. The RE construction technique consists of superimposing layers of moistened and compacted raw earth inside a formwork. It should be noted that the main binder used in traditional unstabilized RE is clay. Subsequently, with industrialization, new modern RE, known as stabilized, were developed by adding other binders, such as cement,

hydraulic lime, or air lime. It should be noted that the main objective of stabilizing of RE is to increase its durability against water and to improve its mechanical performance [2].

RE structures generally offer excellent thermal inertia due to the significant thickness of their monolithic walls and to the hygroscopicity of the earth material, which allows for the successive condensation and evaporation of water, in accordance with variations in external conditions [3]. To the best of our knowledge, a large number of studies have investigated this material, from different aspects, namely its hygrothermal behavior, mechanical characteristics, and durability [2], [4–13]. However, the dynamic behavior of RE structures still requires further investigation [14].

The first exploratory study on the dynamic characteristics of RE buildings was conducted by Bui et al. [15], who examined and identified the dynamic characteristics, such as natural frequencies, mode shapes, and damping. On the other hand, Gomes et al. [16] carried out a numerical study on the seismic resistance of earth buildings in Portugal. They performed a seismic assessment using conventional spectral analysis, which is less realistic than nonlinear approaches. However, no validation steps were performed for the numerical model. It should be noted that the onset and progression of damage were not taken into account.

Regarding the work of Georgios et al. [17], they sought to conduct a seismic assessment of the 17th-century adobe church of Kuño Tambo in the province of Cuzco, in Peru, using an approach that combines visual inspection, acoustic testing, and ambient vibration measurements for the purpose of efficiently characterizing the structural behavior of RE building. To complete their work, they then performed numerical analyses, such as pushover analysis, nonlinear dynamic analysis, and macroblock analysis, according to the requirements of Eurocode 8 and local Standards. As for Bui et al. [18], they investigated two full-scale three-dimensional models of RE walls, with rectangular and L-shaped sections. Then, a time-history analysis was carried out on these models, which were subjected to different seismic excitations. Subsequently, the validity of the adopted numerical model was verified by performing an experimental horizontal loading test, as reported in the literature [19].

Similarly, the results of the study conducted by Nguyen et al. [20] revealed, through numerical simulations that were validated by experimental tests on a reduced-scale compressed earth house, that accurate modeling of interfaces and the integration of reinforced concrete elements, such as belts and interior columns, can significantly improve the seismic resistance of earth structures. This same study also highlighted the importance of integrating Rayleigh damping when analyzing the dynamic behavior of these structures. It is worth noting that Algeria, especially the Tlemcen region, possesses a rich historical heritage. Therefore, appropriate conservation and rehabilitation measures are essential for historic RE structures. In order to succeed in this, it is deemed necessary to increase scientific knowledge of the properties of this material, and to better understand the collapse mechanisms of RE constructions, since the quantitative studies previously carried out on the seismic performance remain limited, particularly at the structural level.

The present study, primarily focuses on the small historic town of Mansourah, built between 1303 and 1336, in the western region of the city of Tlemcen (northwestern Algeria). Today, only the northern and western parts of the ramparts of the historic site of Mansourah still exist, giving this site an irregular trapezoidal shape, with a perimeter of around 4128 meters, as illustrated in the plan in Fig. 1. It is important to note that the adobe walls, about 1.50 m thick and 12 m high, were originally surrounded by 80 towers to the east and south, which have almost completely disappeared. The site of the ruins of the ancient Marinid city of Mansourah covers an area of more than 100 ha.

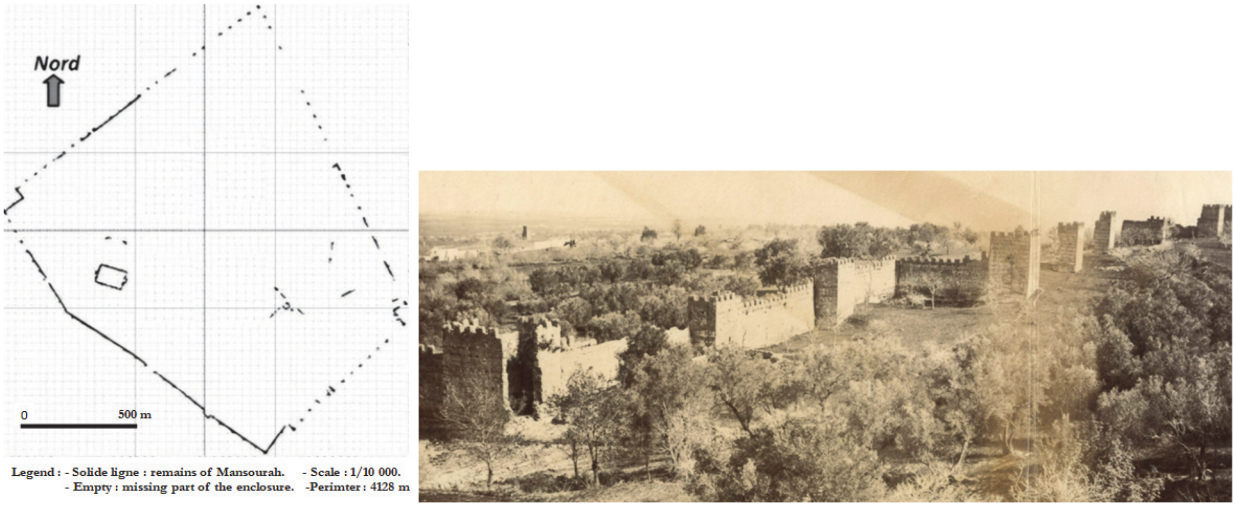

Figure 1: Plane of the enclosure of Mansourah – Tlemcen and a view of a part of the enclosure.

The RE enclosure of Mansourah is a Protected Cultural Property in Algeria. It is classified among the Historical Sites and Monuments (L. 1900), in accordance with Article 62 of Ordinance No. 67-281 of December 20, 1967, published in Official Journal No 7 of January 23, 1968.

This study essentially aims to analyze the seismic response of six representative geometric configurations of the enclosure of Mansourah, through numerical modeling. First of all, some RE core samples taken from the walls of this site were characterized, considering both the physical and mineralogical identification of this material and the results of laboratory mechanical compression and tensile tests, carried out according to the applicable standards [21-27], in order to ensure the reliability of the measured properties.

Subsequently, a nonlinear dynamic analysis was conducted to investigate the seismic behavior of the RE structures constituting the historic enclosure of Mansourah. This analysis was based on the nonlinear time-history analysis method, including an elastoplastic model based on the Drucker-Prager criterion, that was adapted to faithfully represent the response of granular materials under cyclic loading. It should be emphasized that all numerical simulations were performed using the ANSYS Workbench 19.2 (2018) software.

Similarly, the seismic loading was modeled using accelerograms, including an artificial signal compliant with the RPA 2024 specifications for the region of Tlemcen, as well as the actual recording of the earthquake that occurred in Boumerdès on May 21, 2003. This recording was chosen because of its high intensity and its significant impact on buildings in the affected region. Structural damping was modeled using the Rayleigh model. Although rarely applied to RE structures, this approach is essential for realistically assessing the material's capacity to absorb and dissipate vibrational energy.

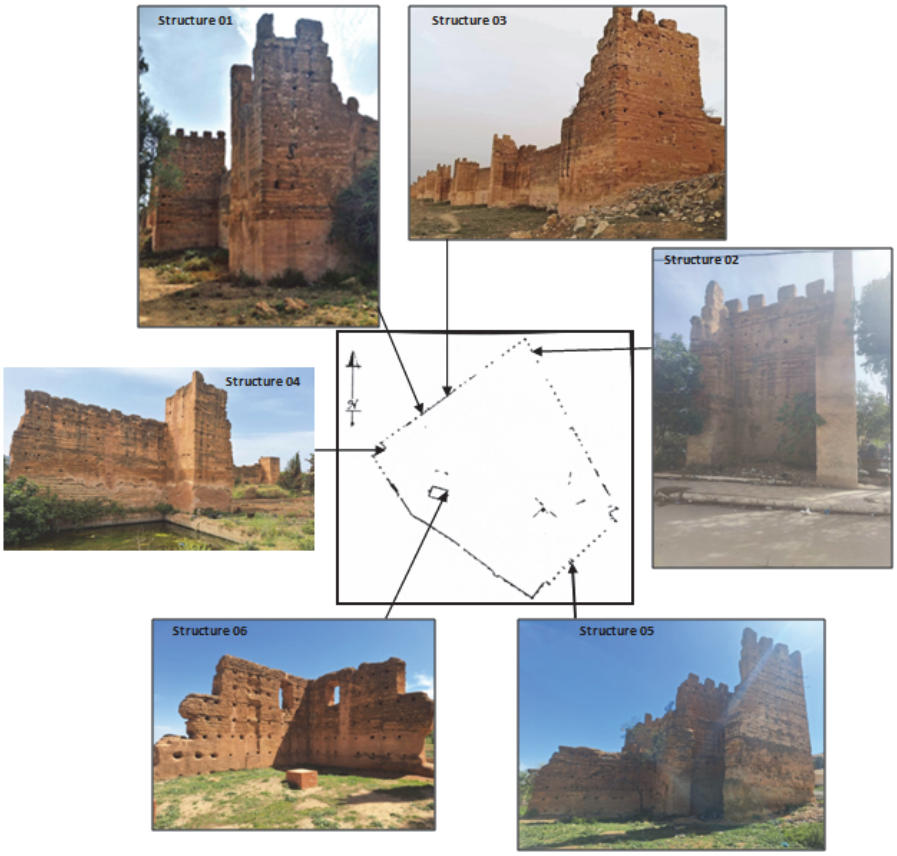

Figure 2: Location of selected structures on the historic site map.

GEOGRAPHIC LOCATION AND DESCRIPTION OF THE STRUCTURES UNDER STUDY

Six representative structural elements of the historic wall of Mansourah were selected for this study. These structures, which are distributed across different parts of the site, exhibit varied geometric configurations. Their precise location is clearly depicted on the site map (Fig. 2). It should be noted that the damages observed on the ramparts

of Mansourah, such as toe erosion, crown erosion, surface erosion, crevices, vertical and stepped cracks, as well as collapsed or ruined sections, are characteristic of structures generally constructed of RE.
A geometric survey was conducted on-site across the different areas to be analyzed, taking into account, as much as possible, all openings and geometric irregularities of architectural origin, or those resulting from deterioration. The following Figs. 3-8 illustrate the geometric shapes and dimensions of the structures selected for our study.

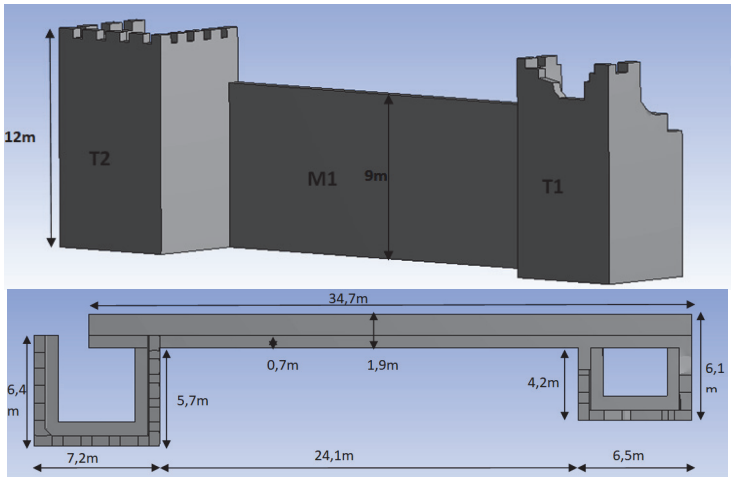

Figure 3: Geometry of Structure 01 (Two towers, T1 T2, with an intermediate wall, M1).

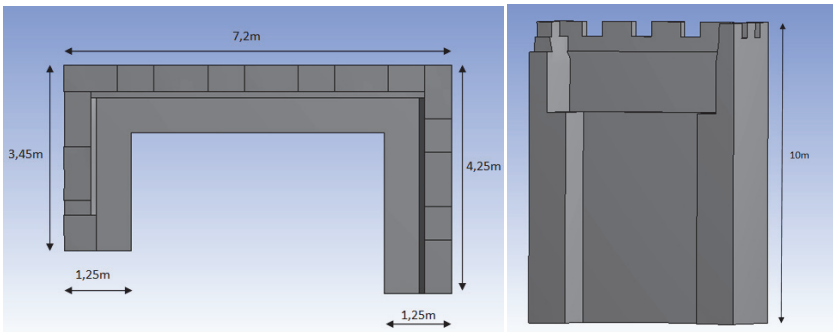

Figure 4: Geometry of Structure 02 (Northeast tower).

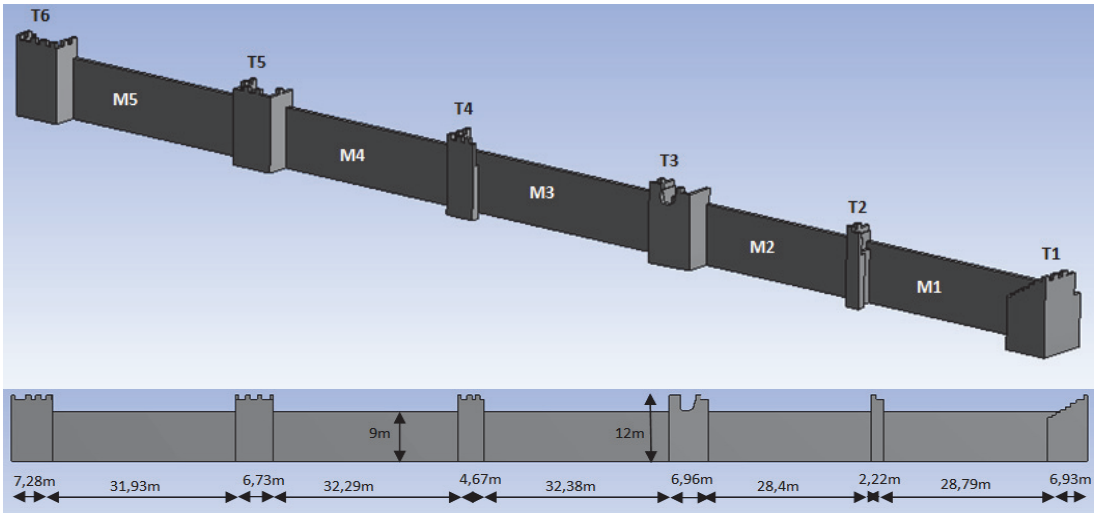

Figure 5: Geometry of Structure 03 (Six towers, T1-T6, linked by intermediate walls, M1-M5).

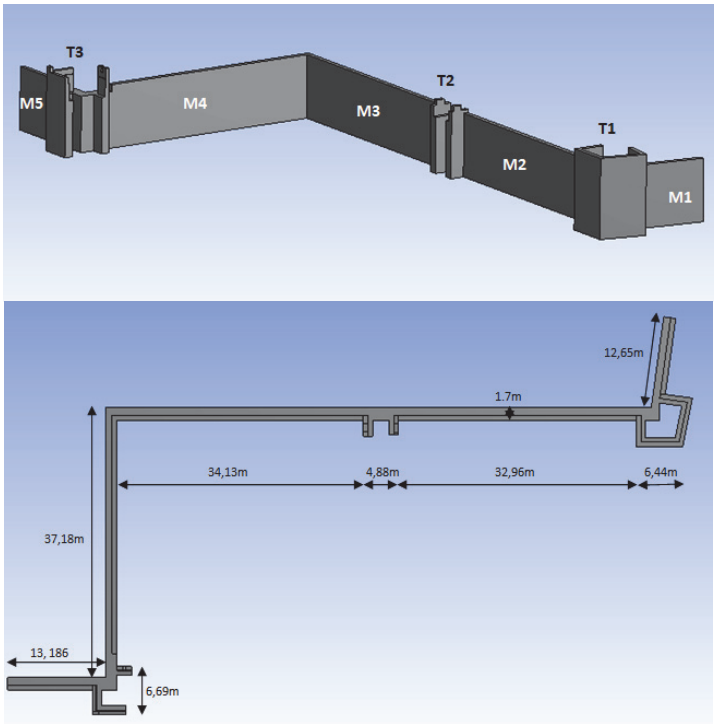

Figure 6: Geometry of Structure 04 (West corner walls, M1-M5, connected to three towers, T1-T3).

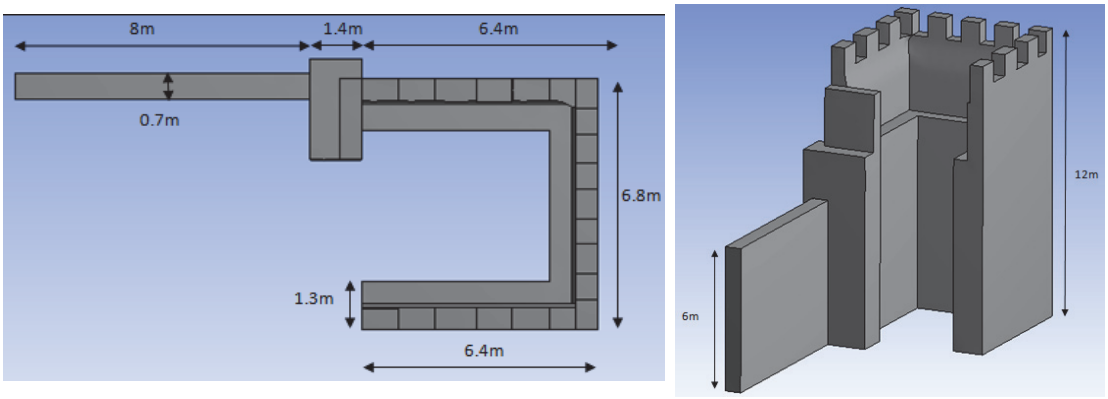

Figure 7: Geometry of Structure 05 (South tower).

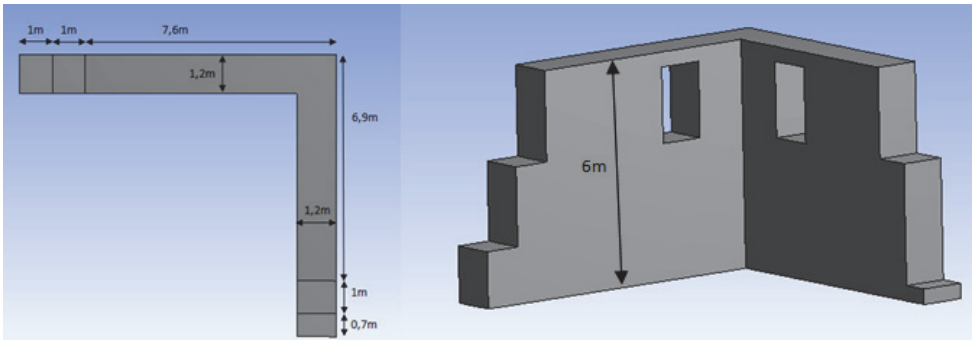

Figure 8: Geometry of Structure 06 (Mosque corner wall).

PHYSICAL, MINERALOGICAL AND MECHANICAL CHARACTERIZATION

Several samples were taken from three different parts of the historic site of Mansourah in order to have a faithful representation of the properties of RE across the entire historical site under study. It is important to emphasize that, due to the historical and heritage importance of the historical site of Mansourah, the sample collection was limited in order to preserve the integrity of the existing structures.

The bulk density of the material is approximately 1424 kg/m³, while its absolute density is about 2160 kg/m³. These values were obtained from samples collected in their natural state. However, the plasticity and liquidity limits could not be determined due to the essentially sandy nature of the material. This characteristic was also confirmed by the methylene blue test, whose values were found to be less than 0.1 (soil with Methylene Blue Value (MBV) < 0.1; according to the GTR 2000 classification system), thus classifying this soil as insensitive to water. Furthermore, the calcite ($CaCO_3$) content of the soil was measured at 47.40% using Bernard's calcimeter test (Standard NF P94-048). All the results of physical identification tests performed on RE material are summarized in Tab. 1.

Sample	Bulk density (kg/m³)	Absolute density (kg/m³)	Bulk density, Hydrostatic weighing (kg/m³)	Liquid limit	Plastic limit	Methylene Blue Value	%$CaCO_3$
1	1426	2150	1550	not measurable	not measurable	0.081	47.40%
2	1426	2170	1555	not measurable	not measurable	0.094	
3	1420	2170	/	not measurable	not measurable	0	

Table 1: Results of the physical identification tests.

Likewise, the soil under study was analyzed using the X-ray diffraction (XRD) technique for the purpose of identifying its mineralogical components. Fig. 9 clearly shows that the analyzed material is mainly composed of calcite ($CaCO_3$) and quartz (SiO_2).

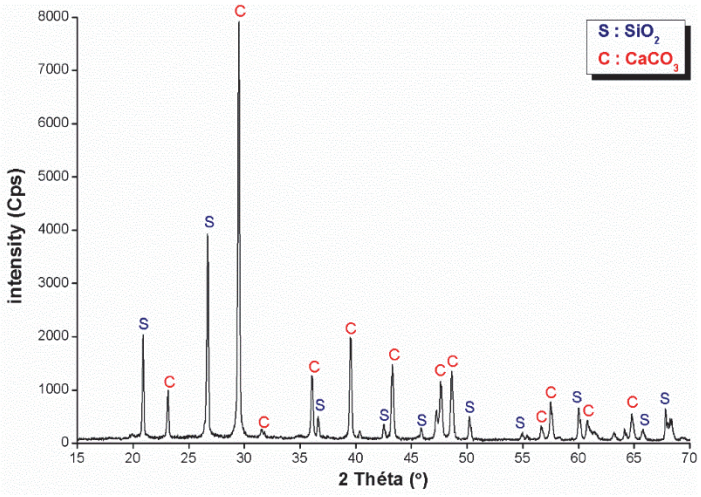

Figure 9: Diffractogram of Rammed Eearth of Mansourah site.

Moreover, the mechanical characterization was carried out to determine the mechanical properties of RE through a series of laboratory tests. Unconfined triaxial compression tests were performed on specimens having a diameter of 50 mm and a height of 100 mm with a view to assess the material's compressive strength (Fig. 10). Fig. 11 shows the variation of the compressive stress as a function of deformation. The shape of the resulting curves is similar to that representing the behavior of an elastoplastic material, typical of cohesive granular materials. The value of the elastic compressive stress was found to be between 1.45 to 2.10 MPa, while the modulus of elasticity varied between 180 and 310 MPa.

Figure 10: Triaxial compression test.

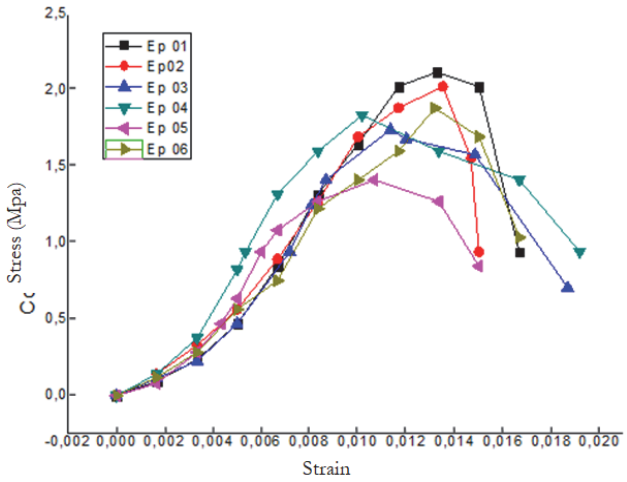

Figure 11: Stress-strain curves.

In addition, indirect tensile tests were carried out on specimens with the same dimensions of D = 50 mm, and H = 100 mm, using the Brazilian method. These tests, as depicted in Fig. 12, made it possible to estimate the tensile strength of the RE. The average value of tensile strength was found to be equal to 0.35 MPa.

Figure 12: Splitting tensile Test.

The state-of-the-art experimental work available in the literature (Tab. 2) has highlighted significant variability in results depending on test conditions, material characteristics, and sample preparation protocols.

Dimensions (cm)	Bulk density (Mv) (kg/m³)	Compressive strength (R_C) (MPa)	Tensile strength (R_T) (MPa)	Young's modulus E (MPa)	Reference
20 x 20 x 40	/	1	0.17	500	Bui et al. [9].
D = 10, H = 20	1850	2.46	/	160	Maniatidis et al. [6].
30 x 30 x 60	1763 - 2170	0.62 – 0.97	/	60 - 70	Maniatidis et al. [6].
50 x 11 x 50	/	3.73	/	4143	Bui et al. [10].
15 x 15 x 15	1870 - 2170	1.8-2	/	/	Lilley et al. [4].
100 x 100 x 30	/	0.6 – 0.7	/	60	Jaquin et al. [13].

Table 2: Summary of work on the mechanical characteristics of rammed earth.

FINITE ELEMENT MODELS

The Mansourah site enclosure was built using tower-reinforced walls (Bordj) whose significant thickness plays a key role in wind bracing of the structure.

Three-dimensional finite element models of six geometric configurations, representative of the historic site, were developed as part of this work using ANSYS Workbench 19.2. These structures are distributed as follows:

- Structure 01: Two towers (T1, T2) with an intermediate wall (M1).
- Structure 02: Northeast tower.
- Structure 03: Six towers (T1-T6) connected by intermediate walls (M1-M5).
- Structure 04: West corner wall, (M1-M5) connected to three towers (T1-T3).
- Structure 05: South tower connected to a wall.
- Structure 06: Corner wall of the mosque.

It is noteworthy that the considerable thickness of the walls, ranging from 1.25 m and 1.90 m across the entire site, gives the structures a high inertia. Furthermore, the RE material, naturally consolidated over nearly eight centuries, exhibits a homogeneous behavior at the macroscopic level. For this reason, it was deemed appropriate to neglect the effect of the interface between the RE layers. This aspect was not taken into account in the numerical modeling.

Given the construction technique associated with Mansourah site, where medium-sized stone is incorporated locally at the base of the wall and remains embedded in the RE structure without forming a distinct base, it was decided to neglect the effect of this foundation rubble during the numerical modeling. The structure was thus modeled as fixed at its base, which corresponds to the architectural and structural reality of the site under study. It should be emphasized that all openings and windows were taken into account in the modeling. Furthermore, the meshing was performed taking into account the geometric complexity of each structure. For structures 01, 02, 05, and 06, the SOLID186 element was used; this is a hexahedral element with 20 nodes and quadratic interpolation. However, for structures 03 and 04, which have complex geometries, the SOLID187 element was adapted. This tetrahedral element with 10 nodes and quadratic formulation allows for efficient meshing of irregular shapes. The geometric and discretization data are summarized in Tab. 3.

Structure	01	02	03	04	05	06
Location on the historic site	North	Northeast	North	Northwest	South	West
Length (m)	37.80	7.20	188.57	94.942	15.80	9.60
Width (m)	7.60	4.25	8.01	54.905	7.35	8.6
Max height (m)	12	10	12	12	12	6
Number of finite elements (F.E.)	39300	20246	74419	45004	13504	18786
Number of nodes	7543	3937	39767	23778	2368	3668

Table 3: Data for the different structures modeled.

The Drucker–Prager elastoplastic criterion, which was implemented in the ANSYS Workbench 19.2 (2018) software, was used to represent the nonlinear behavior of RE. Unlike the classical formulation in geomechanics, which is based on cohesion and friction angle, this version of the software directly uses uniaxial compressive and tensile strengths as input

parameters. This approach has the advantage of more closely linking the numerical simulation to experimental results from simple tests carried out on the material under study. The yield criterion is written in its general form as follows:

$$F(\sigma) = \gamma I_1 + \sqrt{J_2} - K \leq 0 \quad (1)$$

where $I_1 = \sigma_1 + \sigma_2 + \sigma_3$ is the first stress invariant, J_2 is the deviatoric invariant, γ is a weighting coefficient related to internal friction, and K is the ultimate stress related to the cohesion of the material.
These coefficients are directly associated with the compressive (R_C) and tensile strengths (R_T) through the relations given below [28].

$$R_C = \frac{K\sqrt{3}}{1-\gamma\sqrt{3}} \quad (2)$$

$$R_T = \frac{K\sqrt{3}}{1+\gamma\sqrt{3}} \quad (3)$$

The ultimate stress K was determined based on experimental results. Calibration was performed by inputting the measured compressive and tensile strengths into relations (2) and (3), allowing the Drucker–Prager parameters to accurately reflect the mechanical behavior of the material.
Furthermore, the modal analysis was conducted in the elastic regime, while the time-domain dynamic analysis incorporated the plasticity law. The parameters used in the modeling were taken from the experimental results defined previously and they are summarized in Tab. 4.

Material	Bulk density Mv (kg/m³)	Young's modulus E (MPa)	Poisson's ratio ν	Compressive strength R_C (MPa)	Tensile strength R_T (MPa)	Biaxial compressive strength R_B (MPa)
Rammed Eearth	1550	240	0.22	1.8	0.35	2

Table 4: Input parameters of the numerical model as established in the laboratory.

STRUCTURAL ANALYSIS

Dynamic modal analysis

This type of analysis primarily aims to provide a detailed understanding of structural dynamics by determining the significant vibration modes, their natural frequencies and associated modal shapes, as well as the modal participation factor for each direction. In addition, this study also determines the Rayleigh damping coefficients, which are essential for assessing the structures' ability to dissipate the vibration energy.
The modal analysis of all structures was performed using ANSYS Workbench 19.2 software, taking into account twelve vibration modes. The physical and mechanical characteristics of the RE material used are: density, M_v = 1550 kg/m³, Young's Modulus, E = 240 MPa and Poisson's ratio, ν = 0.22.
This analysis provided a better understanding of the vibrational behavior of each structure by identifying the most significant natural modes. The corresponding results are presented in Tab. 5 and in the Figs. 13-18, which illustrate the observed modal shapes.
Structure 01 (Fig. 13): The main mode along the X axis is mode 1, characterized by horizontal translation, with a natural frequency of 1.91 Hz. Similarly, mode 2 is characterized by a translation along the Y axis, with a natural frequency of 2.21 Hz. Finally, mode 5 corresponds to a torsional motion around the Z axis, with a frequency of 3.45 Hz.
Structure 02 (Fig. 14): Vibration modes 1 and 2 are the most significant. These are coupled translational modes along the X and Y directions, characterized by frequencies of 2.49 and 2.75 Hz, respectively. Mode 4 represents a pure translation in the Y-axis direction, with a frequency of 4.63 Hz. The dominant mode along the Z axis is mode 11, with a relatively high frequency of 11.54 Hz.

Structure 03 (Fig. 15): Modes 1 and 2 are two coupled dominant modes characterized by a motion that combines torsion around the Z axis and translation along the Y axis. Mode 1 has a natural frequency of 1.90 Hz, while mode 2 has a natural frequency of 1.97 Hz. The main mode in the X-axis direction is mode 10, which is a pure translation mode with a natural frequency of 2.59 Hz.
Structure 04 (Fig. 16): Mode 1 is the main translation mode along the X axis, with a natural frequency of 1.62 Hz, while mode 2, a coupled translation mode, is dominant in the Y and Z-axis directions, with a frequency of 1.75 Hz. Finally, the main tortional is mode 10, with a natural frequency of 2.66Hz.
Structure 05 (Fig. 17): Mode 4 is the main translation mode along the X axis, with a natural frequency of 3.28 Hz. In the Y-axis direction, mode 1 is dominant, also a translation mode, with a frequency of 1.75 Hz. Finally, the main mode along the Z axis is mode 8, a torsion mode, with a frequency of 5.10 Hz.
Structure 06 (Fig. 18): Modes 3 and 2 are the two main coupled modes characterized by translation along X and Y axes. The values of the natural frequencies, for the two modes, are respectively equal to 3.13 Hz and 3.66Hz. The main mode along the Z-axis direction is mode 11, a torsional mode with a relatively high natural frequency of 17.12 Hz.
Likewise, the modal analysis revealed that the first modes are dominated by horizontal translations, while the higher modes are primarily torsional, with stiffness increasing with frequency. These findings constitute a fundamental step towards better understanding: first, the dynamic distribution of forces, and second, the directional vulnerability of the structures studied.

Structure	Mode	Frequency (Hz)	Period (s)	Participation ratio X	Participation ratio Y	Participation ratio Z
Structure 01	1	1.91	0.52	0.95	0.041	0.18
	2	2.21	0.45	0.056	1	0.45
	5	3.45	0.29	0.62	0.78	1
Structure 02	1	2.49	0.40	0.95	0.72	0.007
	2	2.75	0.36	1	0.84	0.01
	4	4.63	0.22	0.19	1	0.002
	11	11.54	0.07	0.043	0.16	1
Structure 03	1	1.90	0.53	0.23	0.90	0.92
	2	1.97	0.51	0.07	1	1
	10	2.59	0.38	1	0.03	0.28
Structure 04	1	1.62	0.67	1	0.17	0.48
	2	1.75	0.57	0.15	1	0.95
	10	2.66	0.37	0.23	0.28	1
Structure 05	1	1.75	0.57	0.06	1.00	0.03
	4	3.28	0.30	1.00	0.04	0.29
	8	5.10	0.20	0.42	0.42	1.00
Structure 06	1	3.13	0.32	0.94	0.70	0.0007
	2	3.66	0.27	0.72	1	0.009
	3	7.09	0.14	1	0.68	0.06
	11	17.78	0.058	0.25	0.22	0.85

Table 5: Main natural vibration modes.

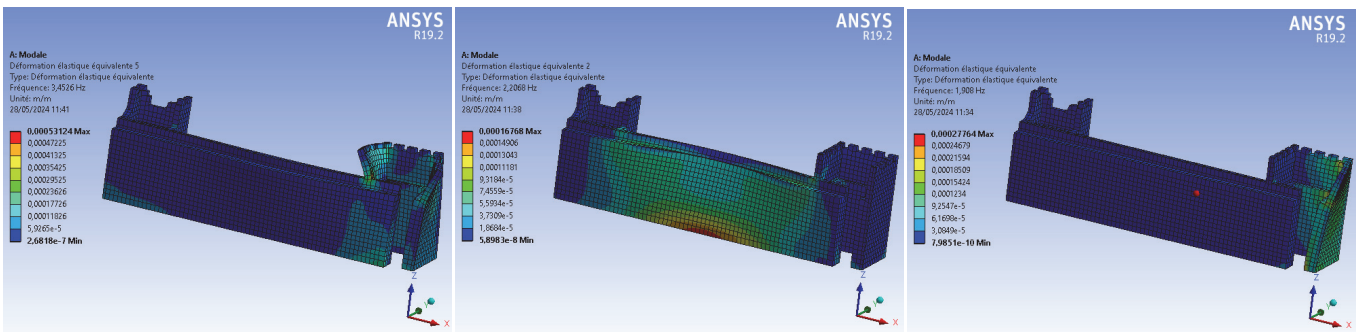

Mode 1, f1=1.91Hz Mode 2, f2=2.21Hz Mode 5, f5=3.45Hz

Figure 13: Main natural vibration modes for Structure 01.

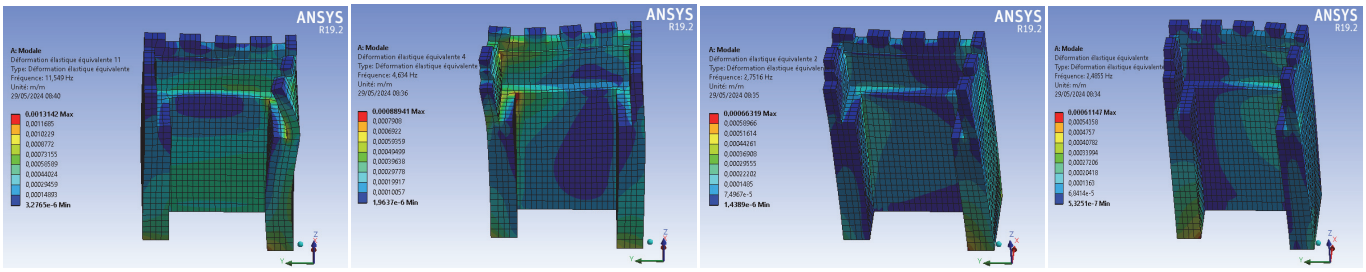

Mode 1, f1=2.49Hz Mode 2, f2=2.75Hz Mode 4, f4=4.63Hz Mode 11, f11=11.54Hz

Figure 14: Main natural vibration modes for Structure 02.

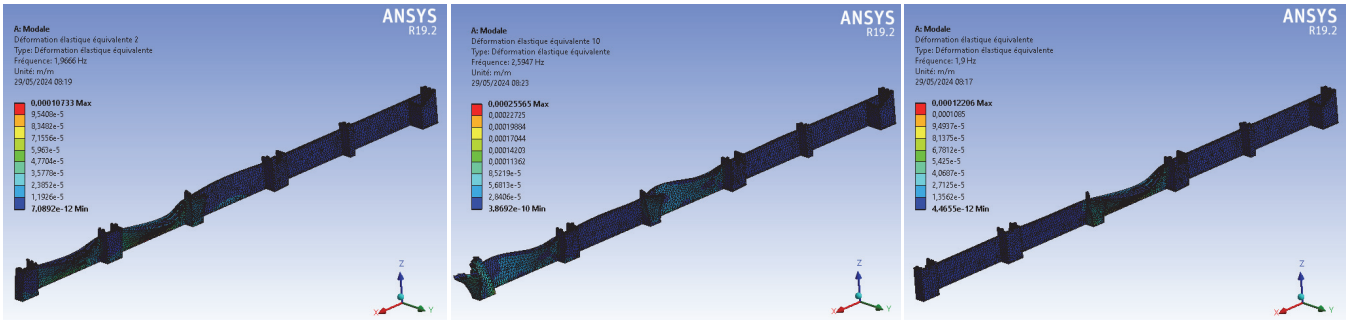

Mode 1, f1=1.90Hz Mode 2, f2=1.97Hz Mode 10, f10=2.59Hz

Figure 15: Main natural vibration modes for Structure 03.

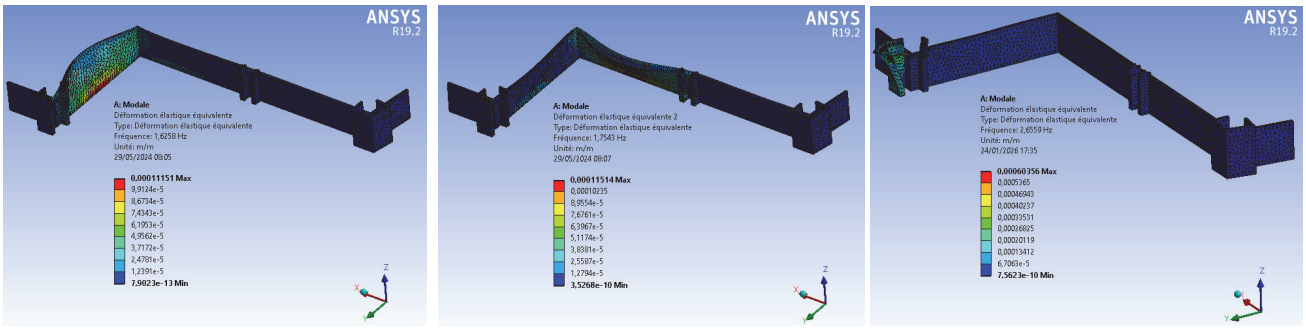

Mode 1, f1=1.62Hz Mode 2, f2=1.75Hz Mode 10, f10=2.66Hz

Figure 16: Main natural vibration modes for Structure 04.

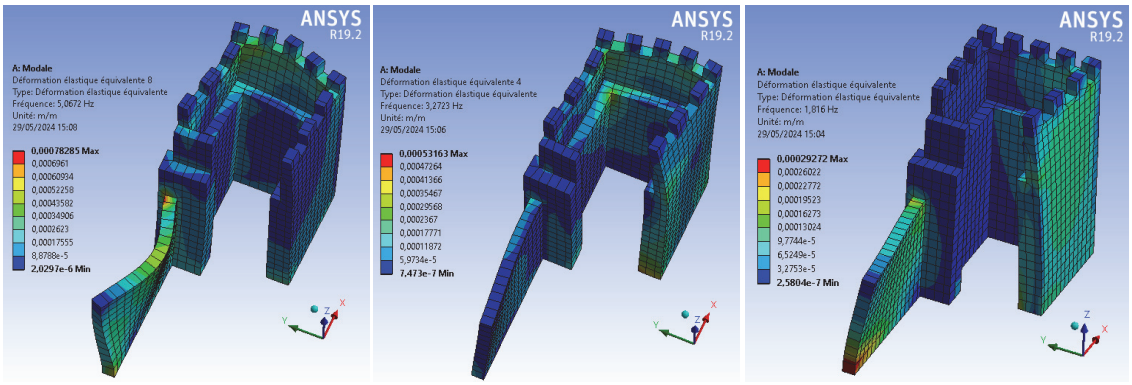

Mode 1, f1=1.75Hz Mode 4, f4=3.28Hz Mode 8, f8=5.10Hz

Figure 17: Main natural vibration modes for structure 05.

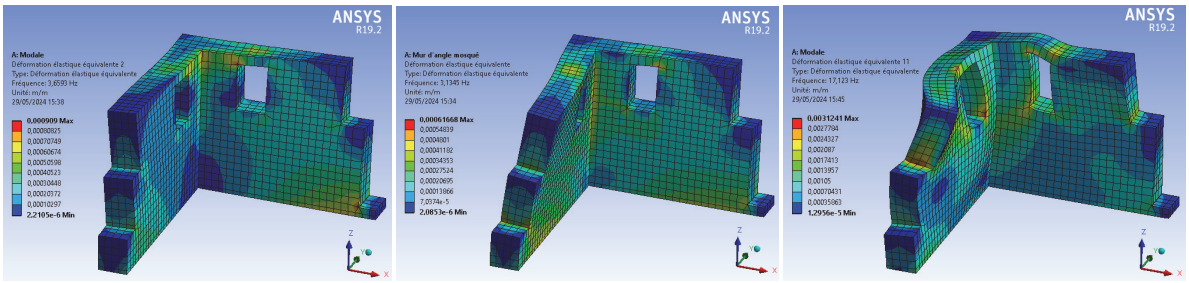

Mode 1, f1=3.13Hz Mode 2, f2=3.66Hz Mode 11, f11=17.78Hz.

Figure 18: Main natural vibration modes for Structure 06.

Time history analysis

The time history analysis method, a nonlinear dynamic approach, was used in this work. It is based on the use of numerical integration methods to solve the equation of motion at each time step and to achieve an accurate and realistic analysis of the complex behavior of the materials composing the structure. This method, although is more complex and requires more computational resources, offers a fairly realistic and detailed assessment, making it functional for complex structures that require in-depth analysis.

Two accelerograms were used to better understand the dynamic behavior of RE structures at Mansourah site, which is considered in the present case. The first one is an artificial accelerogram representative of the city of Tlemcen, generated from an elastic response spectrum, in accordance with the recommendations of Algerian Seismic Code RPA-2024 (Fig. 19). The second is the actual recording of the north-south component of Boumerdès earthquake, whose magnitude was 6.8 on the Richter scale, recorded on May 21st, 2003 at the Station of Dar El Beida (Algiers) (Fig. 20). This earthquake is one of the most destructive earthquakes in Algeria's recent history. Its epicenter was located near the town of Zemmouri, about 60 kilometers east of Algiers, in the region of Boumerdès.

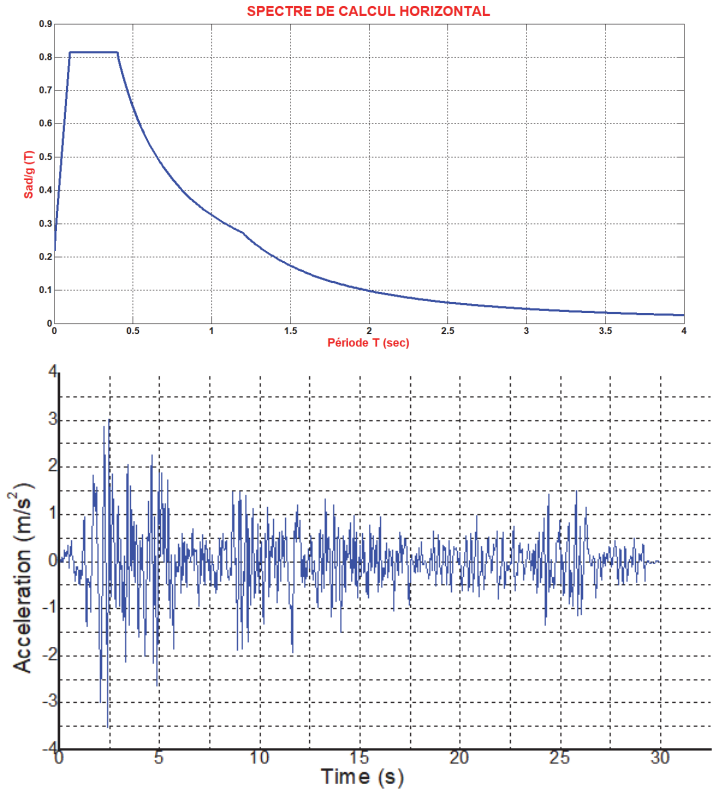

Figure 19: Artificial accelerogram generated from an elastic response spectrum representing the city of Tlemcen.

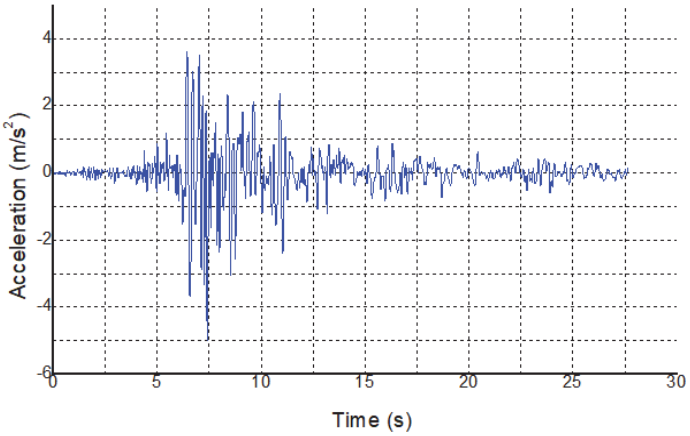

Figure 20: Recordings of the Boumerdes earthquake of May 21st, 2003, at the Dar El Beida station, North-South component.

The damping factor, ξ, is one of the most important parameters in a structure under seismic loading. Damping, in ordinary current structures, is mainly ensured by the deformation of the material (elastic and plastic phases), which dissipates the vibration energy, and by mechanical wave radiation through the medium.
In general, structural damping is rarely considered in research studies on historic buildings, because their damping is often lower than that of modern buildings. This could underestimate the level of structural failure [29].
The Rayleigh method was used in this study. This method is a damping modeling technique in which the damping matrix (C) is a linear combination of the mass matrix (M) and stiffness matrix (K), as indicated by the following equation:

$$C = \alpha M + \beta K \tag{4}$$

with α and β damping factors.
The RE structures were modeled using Rayleigh damping factors, which were calculated first based on an overall damping factor of 4%, as determined by [23] for RE walls, and then on the results of modal analyses that take into account the natural frequencies of the main modes. These coefficients are calculated as follows:

$$\alpha = 2\xi\omega_i \cdot \omega_j / (\omega_i + \omega_j) \tag{5}$$

$$\beta = 2\xi / (\omega_i + \omega_j) \tag{6}$$

where ξ is the damping ratio, which is assumed to be equal to 4% in the dynamic analysis, and ω_i and ω_j are angular vibration frequencies. Tab. 6, given below, summarizes the Rayleigh damping factors for the different structures under study.

Structure	Axis X		Axis Y	
	Damping factor (αx)	Damping factor (βx)	Damping factor (αy)	Damping factor (βy)
Structure 01	0.659	0.0021	0.6767	0.0022
Structure 02	0.656	0.0024	0.8678	0.0017
Structure 03	0.646	0.0025	0.4857	0 .0033
Structure 04	0.4570	0.0034	0.4413	0.0036
Structure 05	0.880	0.0018	0.5990	0.0023
Structure 06	1.0900	0.0012	1.2500	0.0011

Table 6: Rayleigh damping factors for the structures considered in this study.

RESULTS AND DISCUSSION

The distribution of maximum principal compressive and tensile stresses was verified throughout all the structures studied, along the two directions of application (X and Y axes) of the seismic signals from Tlemcen and Boumerdès. This made it possible to identify the zones where the stress concentration exceeds the permissible thresholds, based on the laboratory tests that were conducted on core samples from the historical site under consideration, in order to identify the most critical structural weaknesses.

As part of this study, it was decided to adopt an elastoplastic model with the Drucker-Prager yield criterion to model the nonlinear behavior of RE. However, the ANSYS software displays, by default, the Von Mises equivalent stress, which is better suited for ductile materials, but is not representative of RE. To achieve this, an equivalent constraint, σ_{eq}^{DP}, specific to the Drucker–Prager criterion, was introduced in the post-processing phase through a user-defined result. This constraint is a function of the principal stresses and the coefficient γ, as shown in the equation below:

$$\sigma_{eq}^{DP} = \gamma\left(\sigma_1 + \sigma_2 + \sigma_3\right) + \sqrt{\frac{(\sigma_1 + \sigma_2)^2 + (\sigma_2 + \sigma_2)^2 + (\sigma_3 + \sigma_1)^2}{6}} \tag{7}$$

Plasticization occurs when $\sigma_{eq}^{DP} \geq K$.

Then, the equivalent plastic strains for each structure, along both X and Y directions, as well as the maximum displacements, were subsequently determined and located.

Structural response under the effect of seismic excitation of Tlemcen

Maximum principal compressive stresses: σ_c

The maximum compressive stresses remain below the permissible stress value, along both X and Y directions of the seismic signal, with a maximum of 1.5 MPa, recorded at the base of Structure 03, which includes six towers connected by intermediate walls along the Y axis. This shows that the structures as a whole do not present any risk of crushing in the high-stress areas.

Maximum principal tensile stresses: σ_T

Analysis of the maximum principal tensile stresses applied to the different configurations revealed a concentration of stresses exceeding the permissible limit in several small and large areas. The distribution and intensity of these stresses are presented, in detail, in Figs. 21-26, which depict the distribution maps of maximum principal tensile stresses for each structure analyzed. Tab. 7 presents the numerical values corresponding to the maximum stresses.

Structures	$\sigma_{T,max}$ (MPa) along X axis	$\sigma_{T,max}$ (MPa) along Y axis
Structure 01	0.469	3.98
Structure 02	0.407	0.436
Structure 03	0.405	4.16
Structure 04	0.454	4.66
Structure 05	0.445	0.624
Structure 06	0.405	4.18

Table 7: Maximum principal tensile stresses $\sigma_{T,max}$.

Regarding Structure 01, which is composed of two towers connected by an intermediate wall, the analysis of the stress distribution shows that, along the X axis, the elastic limit is exceeded at the free lateral wall of T2. These stress exceedances reach a maximum value of 0.47 MPa, particularly at the base and above the height of 8 m, in the area where the wall thickness decreases from 1.30 m to 0.70 m. Similarly, along the Y axis, an exceedance of the maximum with a value of 0.40 is recorded in small areas, in the lower part of the intermediate wall. It should be emphasized that these zones, which are clearly visible on the distribution map for both axes of application of the seismic signal, correspond to

weak points that show a tendency to develop cracks in the event of repeated or high intensity earthquakes. However, the very limited extent of these zones suggests that the risk of widespread damage remains low, with vulnerability being primarily localized at very specific points.

Similarly, for Structure 02 (Northeast tower), exceedances of the maximum allowable stress (maximum value of 0.44 MPa along the Y axis) were also observed. However, these exceedances remain confined to small areas, mainly at the base of the front wall and at the end of the side wall.

Likewise, Structure 03, which consists of six towers connected by intermediate walls, exhibits similar behavior. Indeed, stress exceedances were observed along the two main directions (X and Y) but remained limited to small areas, particularly at the connections between the towers along the X axis, and on the lower part of the connecting walls along the Y axis. The maximum stress value recorded along the Y axis is 0.42 MPa.

Furthermore, the analysis of Structures 04 and 05 highlights a notable peculiarity: the stress concentration exceeds the permissible limit, over large areas. For Structure 04 (corner wall), this stress concentration was observed mainly at the base of the intermediate walls and at free end walls, along the X and Y directions, with a maximum value of 0.47 MPa along the Y axis. Similarly, Structure 05 (south tower connected to a wall) shows extensive stress concentration areas, particularly at the base of the free wall and at the point where the thickness of the tower side wall changes, with a maximum value of 0.624 MPa along the Y axis. This more generalized distribution of stresses, which is clearly visible on the distribution maps, significantly increases the risk of crack development and propagation. These observations therefore corroborate the likelihood of partial or major structural damage.

Finally, Structure 06 (two corner walls) is distinguished by a concentration of stresses that are located in restricted areas of the structure, mainly at the ends of walls. The maximum value recorded along the Y axis is 0.42 MPa

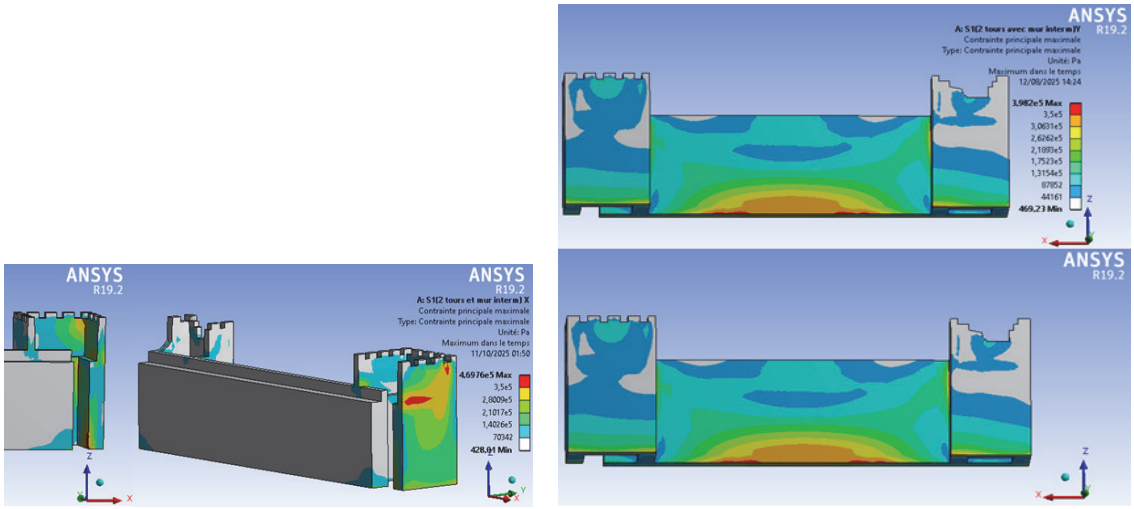

(a) (b)

Figure 21: Concentration of $\sigma_{T,max}$ for Structure 01: (a) Along the X axis, (b) Along the Y axis.

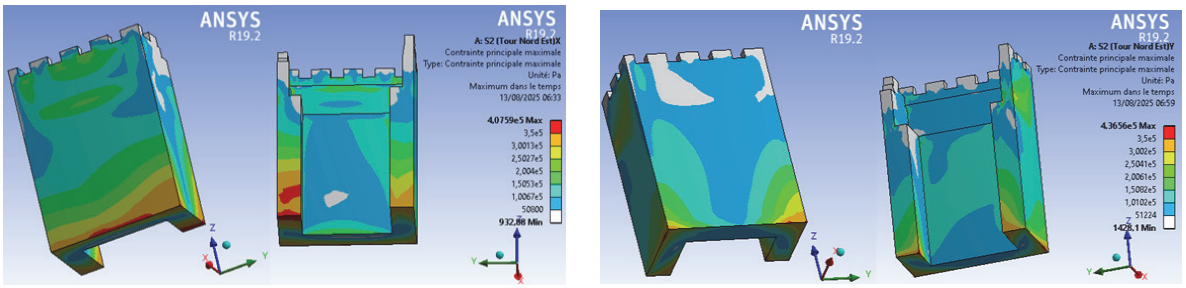

(a) (b)

Figure 22: Concentration of $\sigma_{T,max}$ for Structure 02: (a) Along the X axis, (b) Along the Y axis.

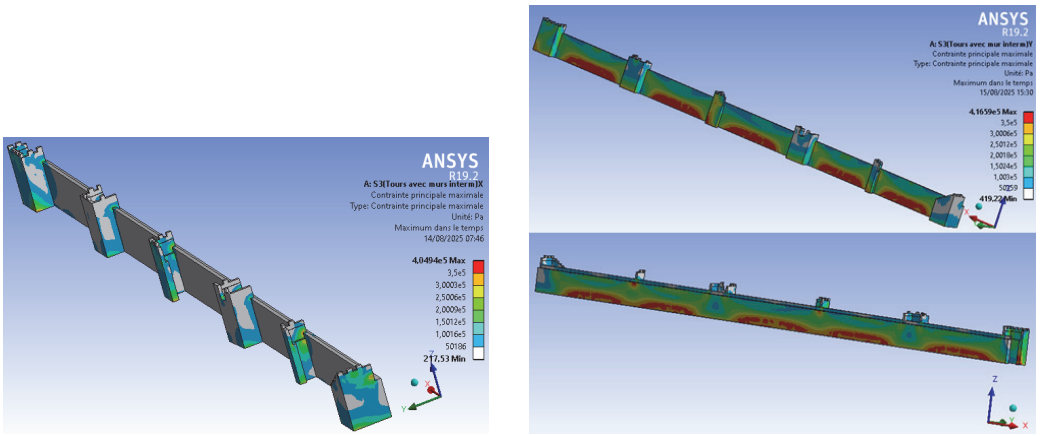

(a) (b)

Figure 23: Concentration of $\sigma_{T,max}$ for Structure 03: (a) Along the X axis, (b) Along the Y axis.

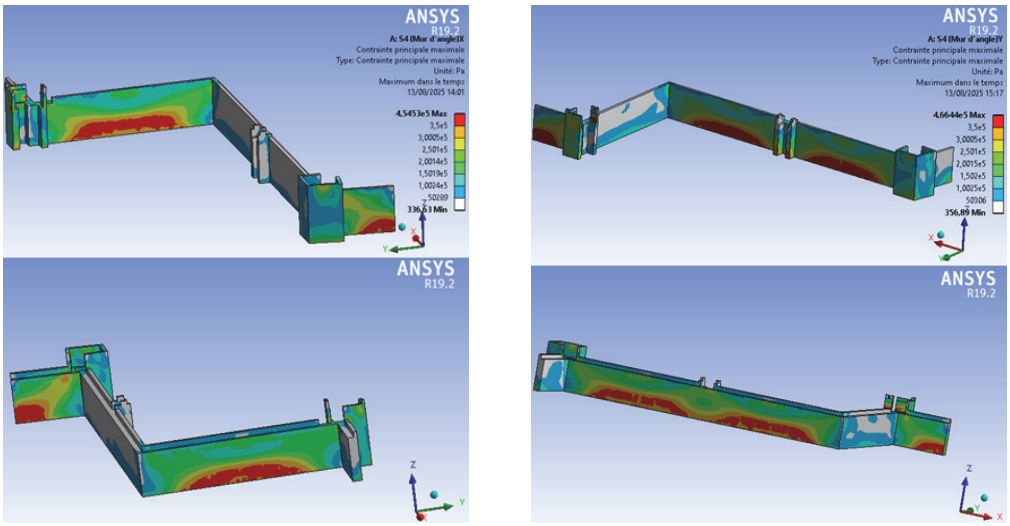

(a) (b)

Figure 24: Concentration of $\sigma_{T,max}$ for Structure 04: (a) Along the X axis, (b) Along the Y axis.

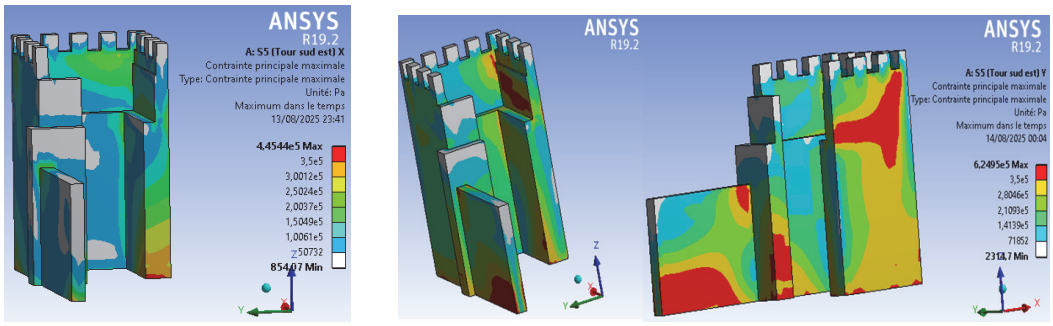

(a) (b)

Figure 25: Concentration of $\sigma_{T,max}$ for Structure 05: (a) Along the X axis, (b) Along the Y axis.

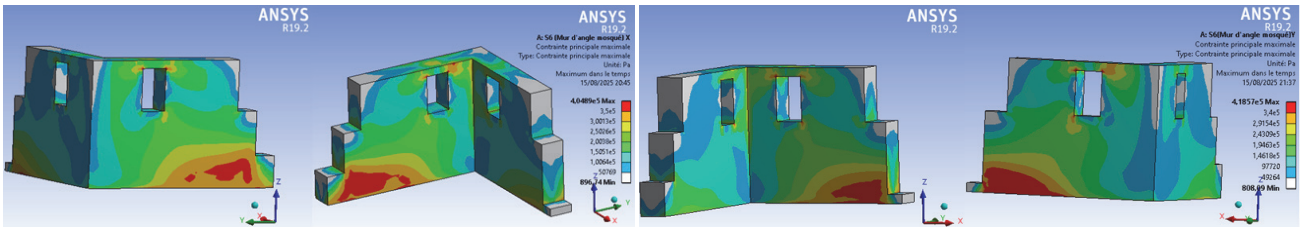

(a) (b)

Figure 26: Concentration of $\sigma_{T,max}$ for Structure 06: (a) Along the X axis, (b) Along the Y axis.

Equivalent stress: σ_{eq}^{DP}

The analysis of equivalent stress, according to the Drucker–Prager criterion, highlights the distributions that are generally consistent with those observed for tensile stress. Exceedances of the admissible thresholds (k = 3.4 MPa) are mainly concentrated at the base of the intermediate walls, at the free end walls, and in areas where the thickness changes, at a height of 8 m on the towers.

Figs. 27-32 depict the equivalent stress distribution maps for all the structures studied. They clearly visualize the position and intensity of the critical zones. Furthermore, Tab. 8 summarizes the corresponding maximum values.

Structures	$\sigma_{eq,max}^{DP}$ (MPa) along X axis	$\sigma_{eq,max}^{DP}$ (MPa) along Y axis
Structure 01	0.454	0.402
Structure 02	0.412	0.432
Structure 03	0.410	0.416
Structure 04	0.439	0.453
Structure 05	0.448	0.645
Structure 06	0.401	0.425

Table 8: Maximum equivalent stress ($\sigma_{eq,max}^{DP}$).

Exceeding the equivalent stress limit does not imply only a risk of localized cracking; it also indicates the beginning of generalized plasticity. The affected areas should therefore be interpreted as zones that may evolve towards irreversible damage with a gradual decrease in load-bearing capacity.

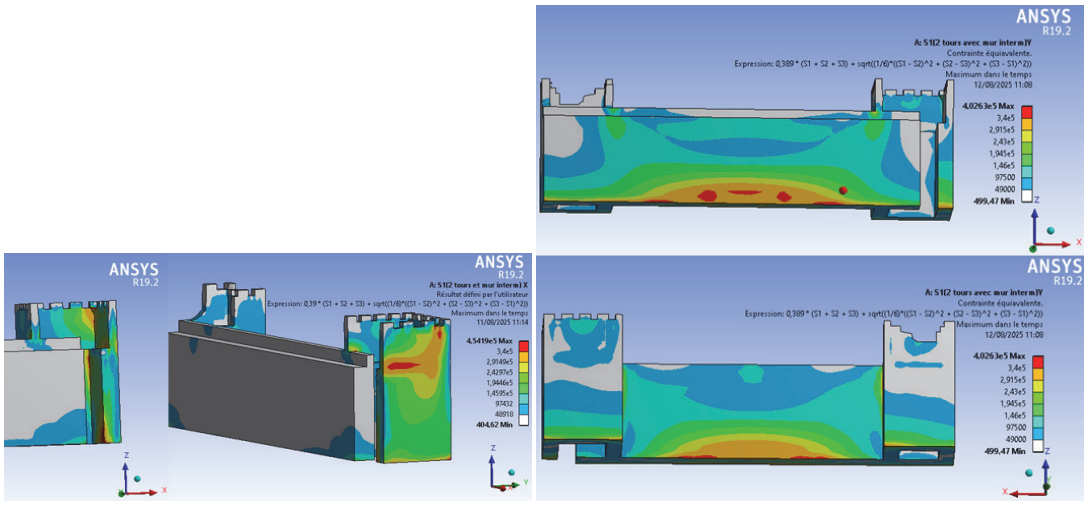

(a) (b)

Figure 27: Concentration of $\sigma_{eq,max}^{DP}$ for Structure 01: (a) Along the X axis, (b) Along the Y axis.

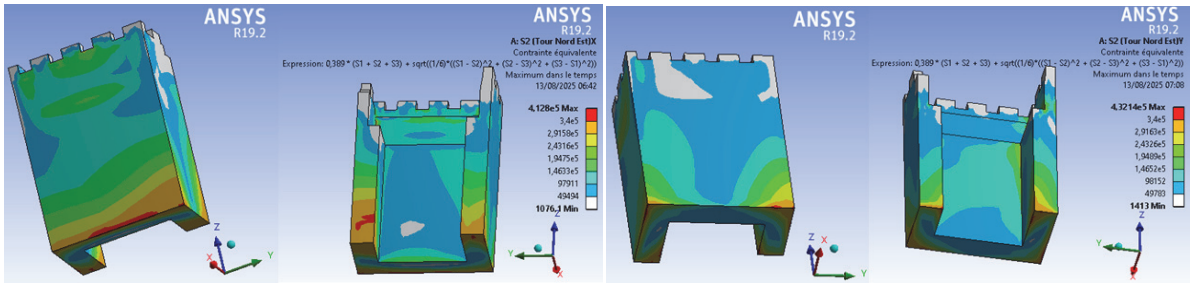

(a) (b)

Figure 28: Concentration of $\sigma_{eq,max}^{DP}$ for Structure 02: (a) Along the X axis, (b) Along the Y axis.

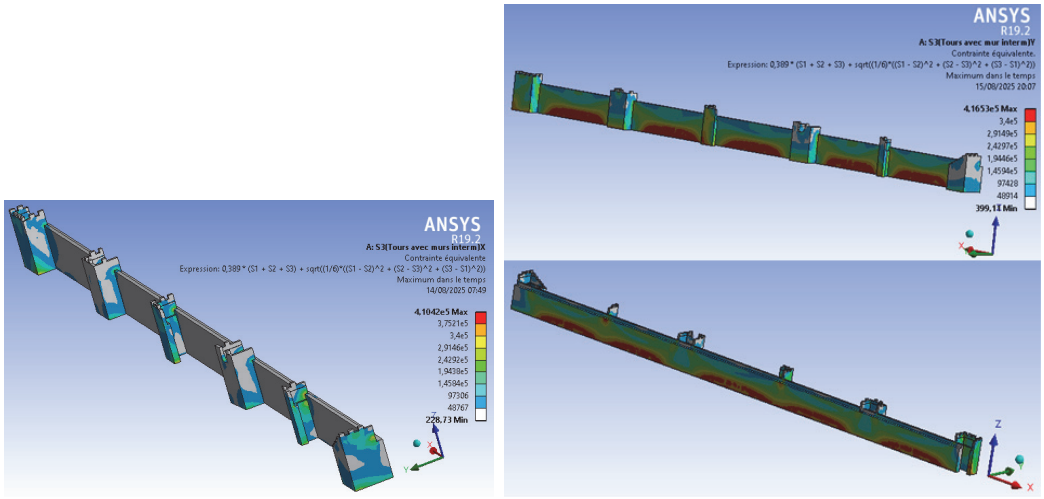

(a) (b)

Figure 29: Concentration of $\sigma_{eq,max}^{DP}$ for Structure 03: (a) Along the X axis, (b) Along the Y axis.

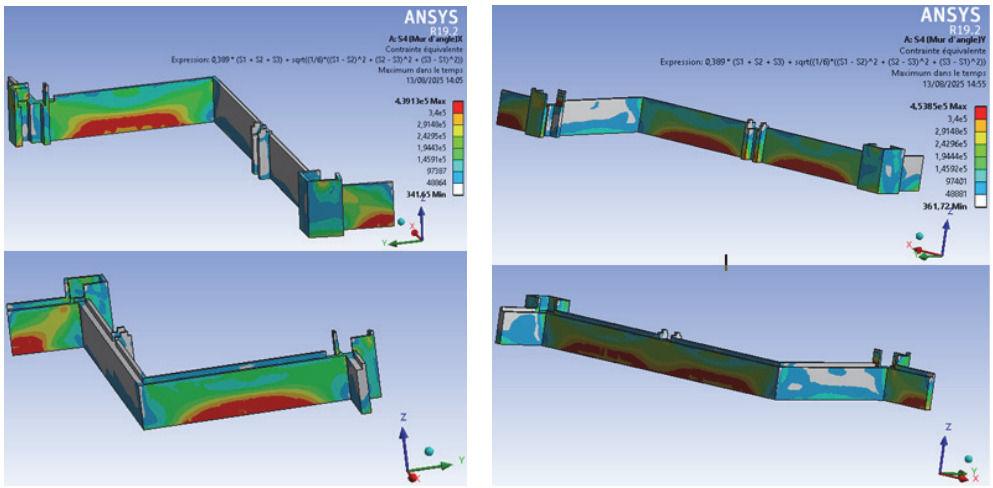

(a) (b)

Figure 30: Concentration of $\sigma_{eq,max}^{DP}$ for Structure 04: (a) Along the X axis, (b) Along the Y axis.

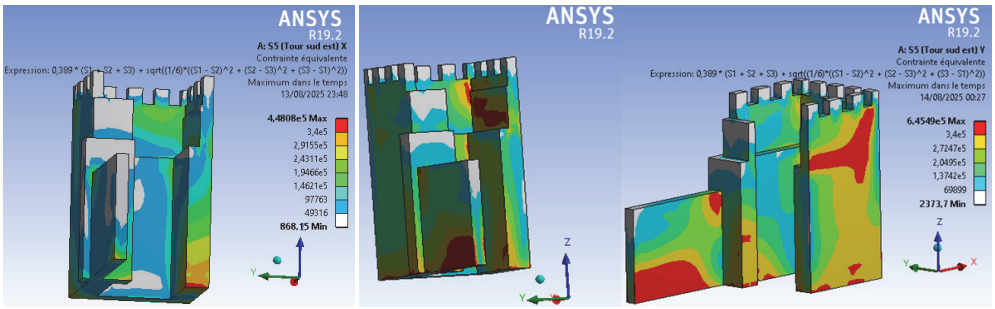

(a) (b)

Figure 31: Concentration of $\sigma_{eq,max}^{DP}$ for Structure 05: (a) Along the X axis, (b) Along the Y axis.

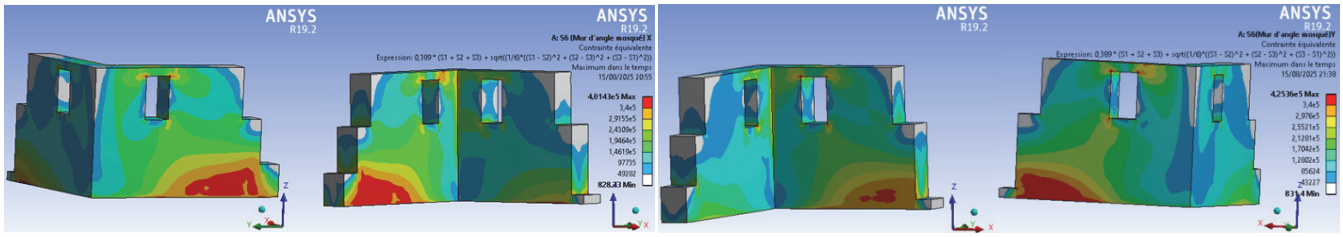

(a) (b)

Figure 32: Concentration of $\sigma_{eq,max}^{DP}$ for Structure 06: (a) Along the X axis, (b) Along the Y axis.

Equivalent plastic deformation: ε_{eq}^{P}

The numerical analysis, conducted on the various historical RE structures, made it possible to identify the concentration zones of equivalent plastic deformation. This equivalent plastic deformation is a fundamental parameter that allows the assessment of localized damage under seismic stress.

Figs. 33-38 show the distribution maps of equivalent plastic strains for all the structures studied and Tab. 9 summarizes the corresponding maximum values.

Structures	$\varepsilon_{eq,max}^{P}$ along the X axis	$\varepsilon_{eq,max}^{P}$ along the Y axis
Structure 01	0.0013	0.00081
Structure 02	0.0037	0.0010
Structure 03	0.0006	0.0014
Structure 04	0.0039	0.0035
Structure 05	0.0022	0.0058
Structure 06	0.0016	0.0018

Table 9: Maximum equivalent plastic deformations $(\varepsilon_{eq,max}^{P})$.

For structure 01, the equivalent plastic strain along the X axis reaches a maximum value of 0.0013 at the lateral wall of tower T2. In contrast, along the Y axis, the strain is mainly concentrated at the base of the intermediate wall, in its central part, with a maximum value of 0.00081.

Regarding Structure 02, the equivalent plastic deformation, along both the X and Y axes, is concentrated mainly at the corners of the tower base. However, a very small volume is affected by this plastic deformation, with maximum values around 0.0037 along the X axis and 0.0010 along the Y axis.

Likewise, regarding Structure 03, for all six towers with intermediate walls, the deformation along the Y axis is localized at the base of the intermediate walls, as well as at the end of the base of the free lateral wall of tower T6, with a maximum value of 0.0014. However, the deformation along the X axis is localized at the connections between wall M1 and tower T1 and between wall M2 and tower T2, with a maximum deformation of 0.0006.

As for Structure 04, concentrations of plastic deformation are observed at the centre of the base of the intermediate walls as well as at the ends of the free walls, along the X and Y directions, with maximum values of 0.0039 along the X axis and 0.0035 along the Y axis.
Regarding Structure 05, the deformation is located mainly at the base of the tower walls, at the height of 8 m, and at the end of the side wall, as well as at the base of the free wall that is connected to the tower, along the Y axis, with a maximum deformation value of 0.0058. On the other hand, the plastic deformation along the X direction is concentrated at the end of the base of the tower's side wall, with a maximum value of 0.0022.
Finally, for Structure 06, the deformation concentration appears at the end of the wall's base, along the X and Y axes, with maximum strains of 0.0016 and 0.0018, respectively.

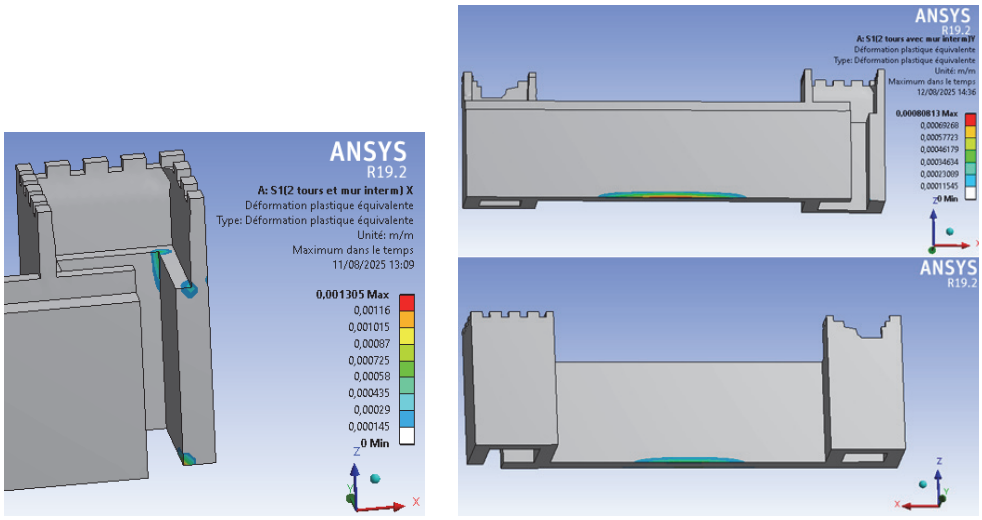

(a) (b)

Figure 33: Equivalent plastic deformation (ε_{eq}^{P}) for Structure 01: (a) Along the X axis, (b) Along the Y axis.

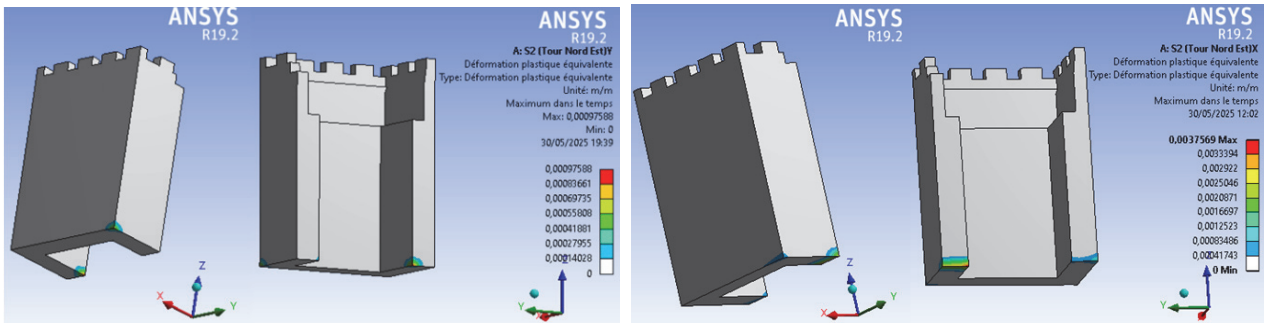

(a) (b)

Figure 34: Equivalent plastic deformation (ε_{eq}^{P}) for Structure 02: (a) Along the X axis, (b) Along the Y axis.

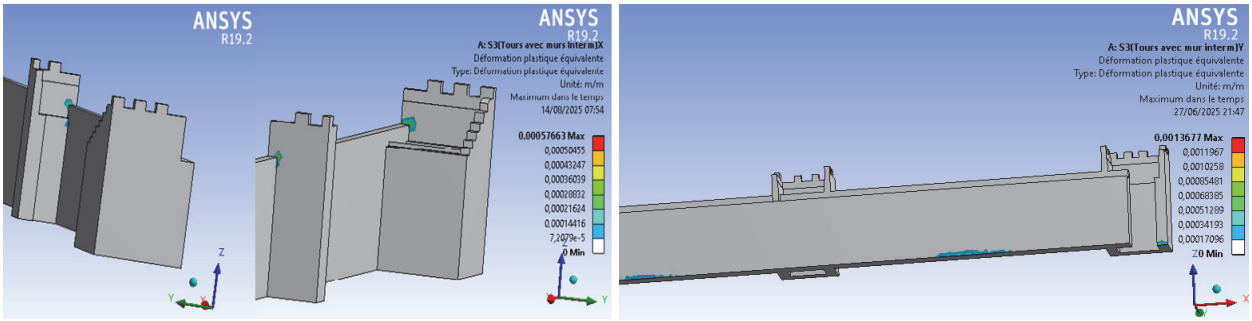

(a) (b)

Figure 35: Equivalent plastic deformation (ε_{eq}^{P}) for Structure 03: (a) Along the X axis, (b) Along the Y axis.

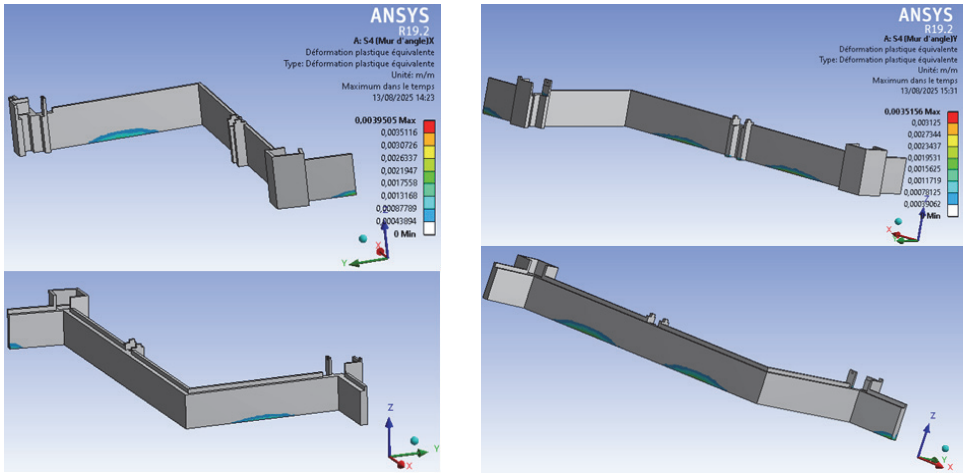

(a) (b)

Figure 36: Equivalent plastic deformation (ε_{eq}^{P}) for Structure 04: (a) Along the X axis, (b) Along the Y axis.

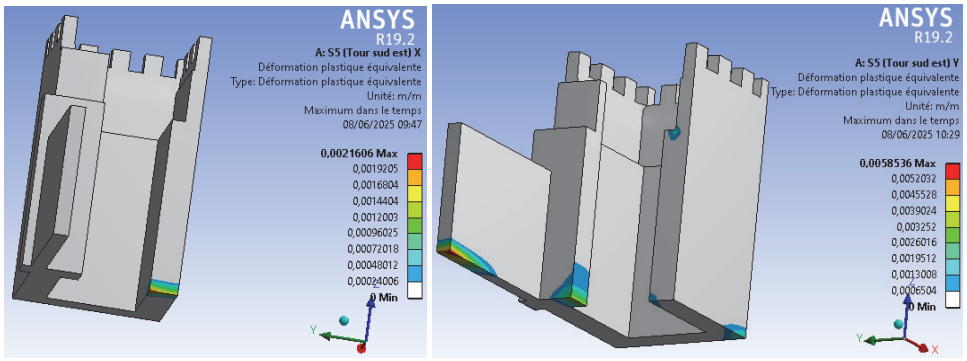

(a) (b)

Figure 37: Equivalent plastic deformation (ε_{eq}^{P}) for Structure 05: (a) Along the X axis, (b) Along the Y axis.

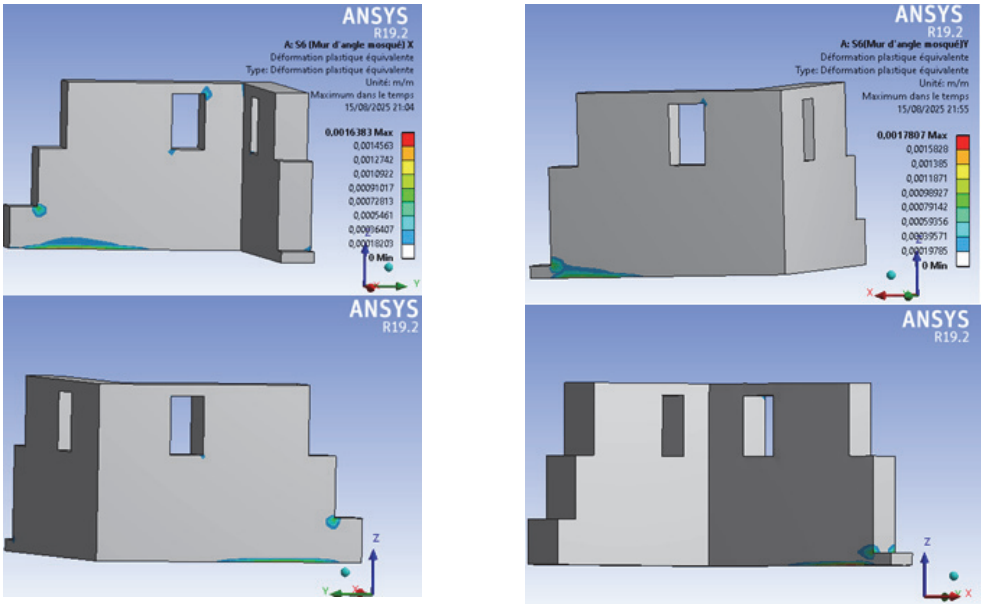

(a) (b)

Figure 38: Equivalent plastic deformation (ε_{eq}^{P}) for Structure 06: (a) Along the X axis, (b) Along the Y axis.

Maximum displacements

Specific control points were defined on each structure:

- Points A were placed at the top of each structure, precisely at the nodes exhibiting maximum displacements.
- Points B were added only for towers where maximum displacements were considered worrisome at 8 m in height, where a reduction in thickness is observed. This was the case for all the structures under study.

Tab. 10 summarizes the coordinates of the control points A and B that were selected on the six structures under study, and the figs.39-44 show the positions of the displacement control points relative to the selected axes.

Structures	Seismic excitation along Y axis						Seismic excitation along X axis					
	A			**B**			**A**			**B**		
	x(m)	y(m)	z(m)	x(m)	y(m)	z(m)	x(m)	y(m)	z(m)	x(m)	y(m)	z(m)
Structure 01	19.15	0	9	-	-	-	0	6.40	12	0	6.40	7.8
Structure 02	0	0	10	-	-	-	0	3.35	10	-	-	-
Structure 03	39.34	0	11	24.8	0	9	0	0	11	-	-	-
Structure 04	14.96	0	9	-	-	-	0	16.5	9	-	-	-
Structure 05	6.4	0	12	6.4	0	7,8	0	3	12	-	-	-
Structure 06	1.7	0	6	-	-	-	0	2	6	-	-	-

Table 10: Coordinates of the displacement control points A and B.

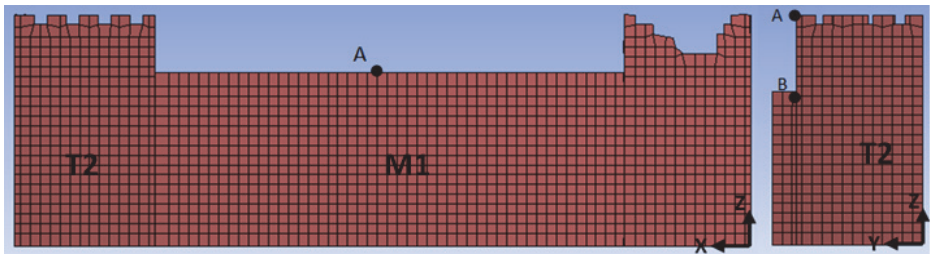

Figure 39: Positions of control points A and B for Structure 01.

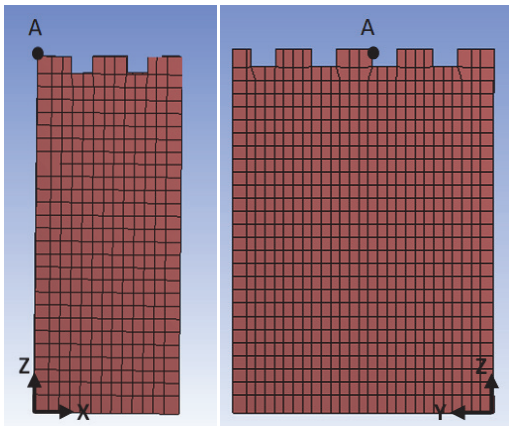

Figure 40: Positions of control points A and B for Structure 02.

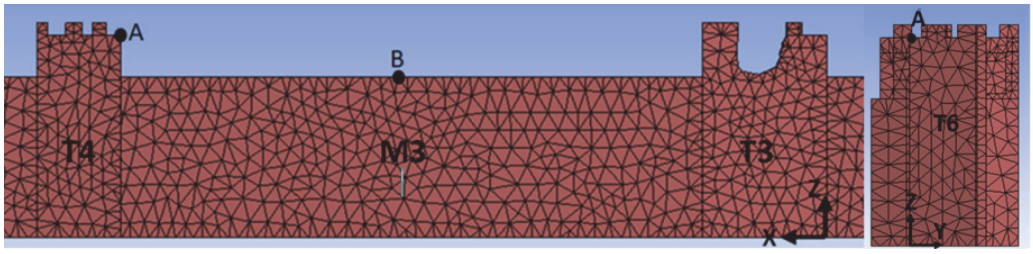

Figure 41: Positions of control points A and B for Structure 03.

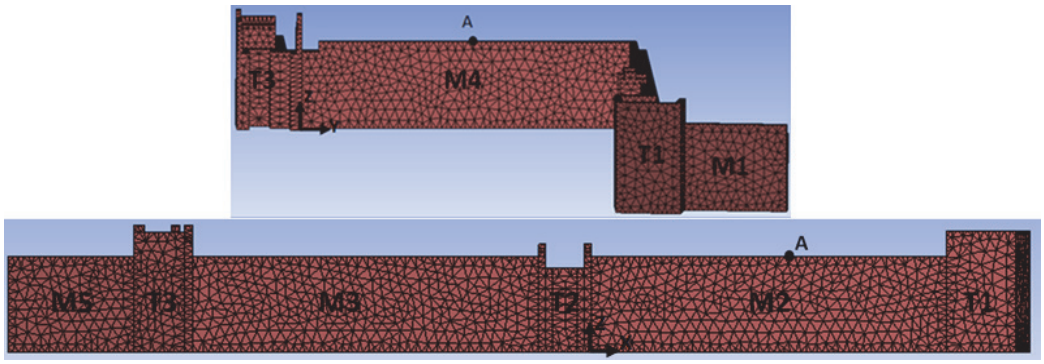

Figure 42: Positions of control points A and B for Structure 04.

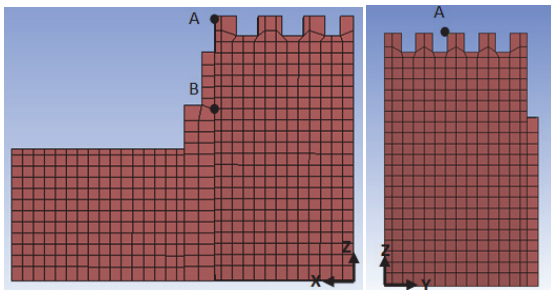

Figure 43: Positions of control points A and B for Structure 05.

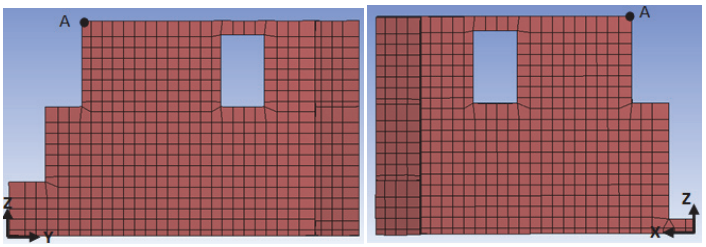

Figure 44: Positions of control points A and B for Structure 06.

The maximum horizontal displacements obtained for the six modeled structures show significant variations which depend on the geometric configuration, wall height, and the position of the geometric weakness zones. Tab. 11 presents the maximum displacements at control points A and B, and Figs.45-50 illustrate the variation of the displacement at points A for all the structures studied.

Structures	Max. disp. (cm) along X axis		Max. disp. (cm) along Y axis	
Structure 01	9.8 (point A)	4.45 (point B)	4.54 (point A)	-
Structure 02	4.13 (point A)	-	4.30 (point A)	-
Structure 03	4.19 (point A)	-	9.27 (point A)	7.60 (point B)
Structure 04	9.76 (point A)	-	9.40 (point A)	-
Structure 05	4.12 (point A)	-	13.4 (point A)	5.79 (point B)
Structure 06	3.82 (point A)	-	3.37 (point A)	-

Table 11: Maximum displacement values at the control points A and B.

For Structure 01 the maximum displacement reaches 4.54 cm along the Y axis at control point A at a height of 9 m. The higher displacement value of 9.8 cm was recorded along the X axis at the top of tower T2, at point A at a height of 12 m, at the free end of the side wall. It should also be noted that in tower T2 there is a low resistance zone that is due to the decrease in thickness between control point B (8 m) and control point A (12 m). The thickness in this zone decreases from 1.25 m to 0.7 m.

Furthermore, Structure 02 exhibits similar displacements in both directions, namely 4.13 cm and 4.30 cm along the X and Y axes, respectively, at the top (point A at 12 m). These low values, which are symmetrical in both directions, suggest good lateral confinement with a relatively rigid seismic response.

As for Structure 03, the maximum displacements, in Y direction, reach 7.60 cm at the top of intermediate wall M3, at point B at a height of 9 m, and 9.27 cm at the top of tower T4, at point A at a height of 11 m. On the other hand, in the X direction, the maximum displacement is 4.19 cm at the top of tower T6, at a height of 12 m, indicating an asymmetrical response along the main axes.

Regarding Structure 04, comparable displacements were recorded in both directions, namely 9.76 cm along the X axis, i.e. wall M3 at a height of 9 m, and 9.40 cm along the Y axis, i.e. wall M1 at a height of 9 m.

In contrast, Structure 05 exhibits asymmetrical behavior, with a displacement of 4.12 cm along the X axis at point A, at a height of 12 m, and a larger displacement along the Y axis, reaching 13.4 cm at the top of the side wall at the same point. Moreover, at point B, located at a height of 8 m, i.e. the zone of thickness decrease, the displacement is 5.79 cm, which further highlights the vulnerability of these thickness reduction zones to deformation.

Finally, Structure 06 exhibits moderate displacements, i.e. 3.82 cm along the X axis and 3.37 cm along the Y axis, measured at the top of the walls, at a height of 6 m (points A). These low values are due to the reduced height and angled configuration of the structure, which is likely to provide its lateral stability.

The findings confirm the strong correlation that exists between displacements and the geometry of the structures. It was found that the free-end walls and geometric transition zones, i.e. thickness reduction, concentrate the highest displacements. In addition, the partially enclosed structures exhibit increased drifts. Conversely, structures with lateral embeddings show better resistance. These observations highlight the need to integrate the geometric shape criteria, thickness discontinuities, and connections between the different elements during the seismic assessment of historic RE structures.

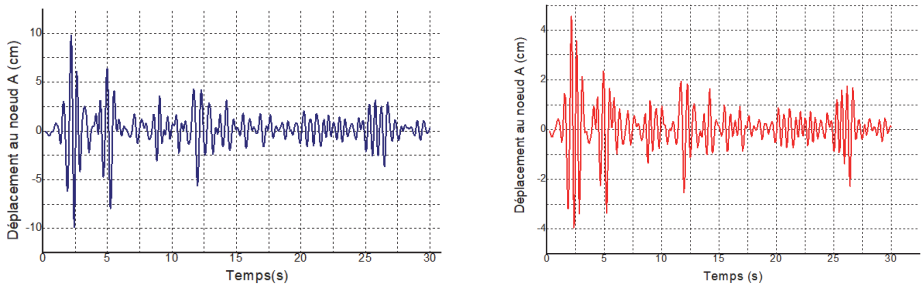

(a) (b)

Figure 45: Horizontal displacement at nodes A: (a) along the X axis, (b) along the Y axis (Structure 01).

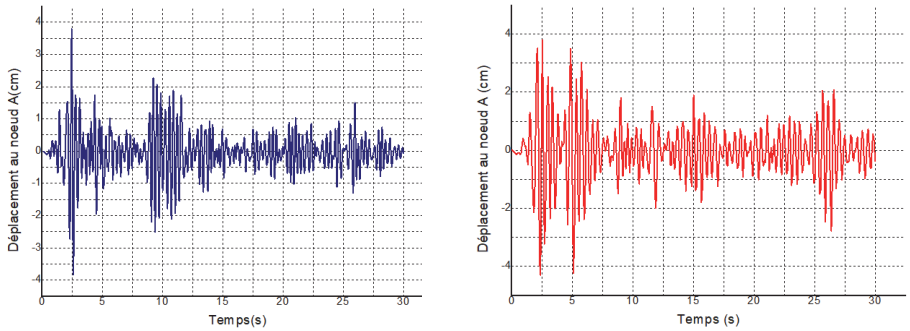

(a) (b)

Figure 46**:** Horizontal displacement at nodes A: (a) along the X axis, (b) along the Y axis (Structure 02).

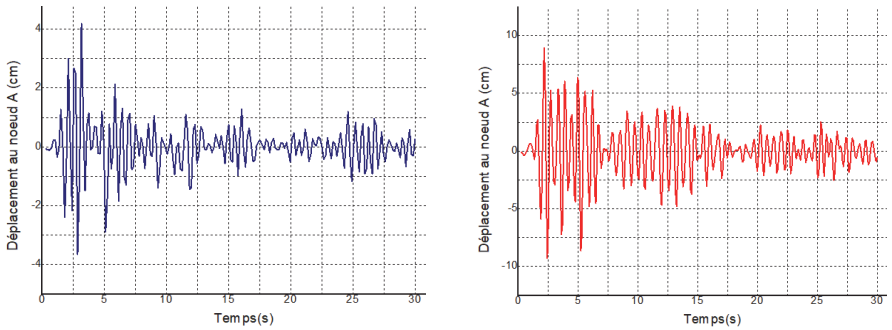

(a) (b)

Figure 47: Horizontal displacement at nodes A: (a) along the X axis, (b) along the Y axis (Structure 03).

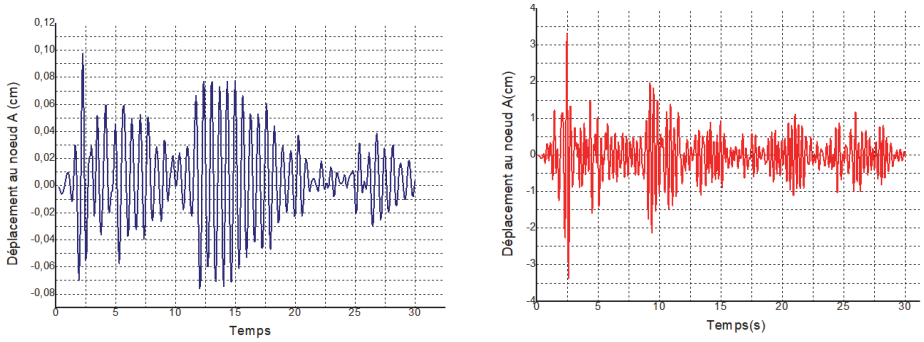

(a) (b)

Figure 48: Horizontal displacement at nodes A: (a) along the X axis, (b) along the Y axis (Structure 04).

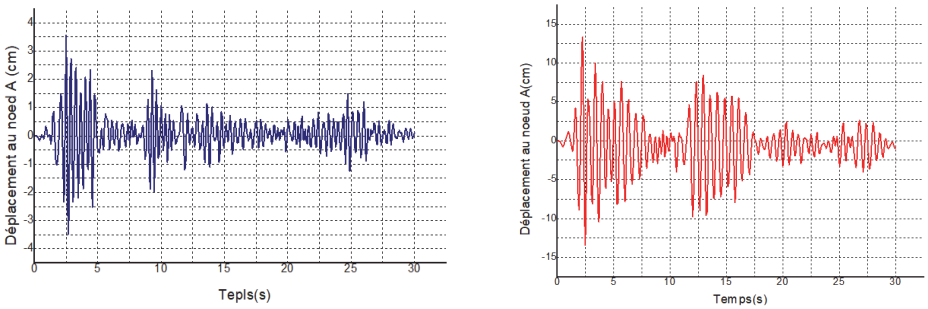

(a) (b)

Figure 49: Horizontal displacement at nodes A: (a) along the X axis, (b) along the Y axis (Structure 05).

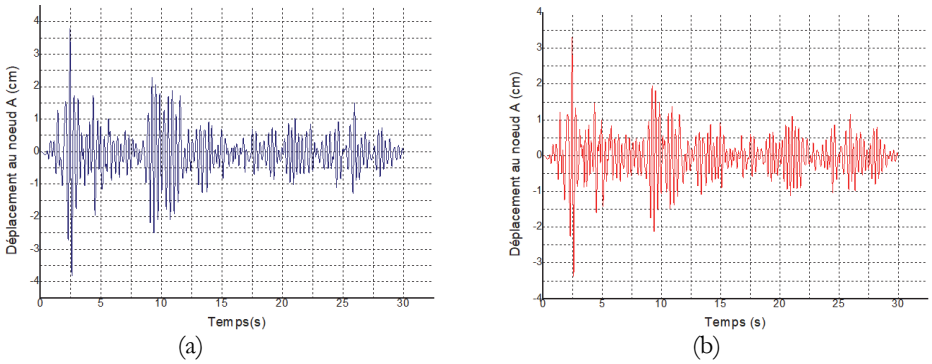

(a) (b)

Figure 50: Horizontal displacement at nodes A: (a) along the X axis, (b) along the Y axis (Structure 06).

Comparative Analysis of Different Geometric Configurations

The numerical evaluation of the six configurations under study, based on the principal tensile and compressive stresses, equivalent stresses, equivalent plastic deformation, and maximum displacements, revealed differentiated behaviors under seismic loading. The findings suggest that, for all structures, the results obtained exceed the permissible thresholds used for historical RE, i.e. 0.35 MPa in tension and 0.34 MPa in equivalent stress, which reflects the material's general vulnerability to tensile forces and combined stress states. However, it should be noted that the magnitude of the exceedances, as well as the displacements and plasticization, varies significantly from one configuration to another. Tab. 12 summarizes the maximum values of the mechanical responses for the six configurations studied in the case of the Tlemcen earthquake.

Structures	$\sigma_{c,max}$(MPa)		$\sigma_{T,max}$ (MPa)		$\sigma_{eq,max}^{DP}$		Max. displacement (cm)		$\varepsilon_{eq,max}^{p}$	
	X Axis	Y Axis	X Axis	Y Axis	X Axis	Y Axis	X Axis	Y Axis	X Axis	Y Axis
Structure 01	0.678	0.574	0.469	3.98	0.454	0.402	9.8	4.54	0.0013	0.00081
Structure 02	1.18	0.0632	0.407	4.36	0.412	0.432	4.13	4.30	0.0037	0.0010
Structure 03	0.614	1.5	0.405	4.16	0.410	0.416	4.19	9.27	0.0006	0.0014
Structure 04	1.33	1.36	0.454	4.66	0.439	0.453	9.76	9.40	0.0039	0.0035
Structure 05	0.939	1.17	0.445	0.624	0.448	0.645	4.12	13.4	0.0022	0.0058
Structure 06	0.773	0.885	0.405	4.18	0.401	0.425	3.82	3.37	0.0016	0.0018

Table 12: Maximum values of mechanical responses of the six configurations studied, in the case of the earthquake of Tlemcen.

The results indicate that the Structure 05 is the most critical, with a significant exceedance in tensile stress (1.78 times the admissible value), and in equivalent stress (1.90 times), with a maximum displacement of 13.4 cm and the higher yielding (ε_{eq}^{P}= 0.0058). Next comes the Structure 04 with notable exceedances of the admissible stresses (σ_T = 1.30 times, σ_{eq}^{DP} = 1.33 times), along with a significant displacement of 9.76 cm and a marked yielding (ε_{eq}^{P} = 0.0039). As for the Structure 01, it is found in an intermediate position, with similar exceedances (σ_T = 1.34 times and σ_{eq}^{DP} = 1.34 times) and displacements around 10 cm, but more limited plasticization, which indicates a relatively more resistant behavior. Next, the Structures 03, 02 and 06 exhibit moderate exceedances of the allowable stresses, with respectively higher and lower maximum displacements (9.27 and 4.13, 3.37) and relatively low yield values. These results indicate that, although local cracking and damage are likely to occur in these cases, the risk of overall instability remains relatively low.

Therefore, the vulnerability ranking of the six configurations, from most vulnerable to most stable, is as follows: Structure 05, 04, 01, 03, 02, 06. This ranking indicates that geometry has an impact on the seismic response of RE structures; it can also be used for the prioritization of restoration and strengthening actions to be initiated.

Structural response under the effect of the seismic excitation of Boumerdès

When the structures under study are subjected to the conditions of Boumerdès earthquake, which is characterized by a magnitude much higher than that of Tlemcen, they generally exhibit an amplified seismic response, hence reflecting a more energetic vibration. However, some configurations, particularly the one corresponding to Sstructure 05, exhibit slightly higher local values under the earthquake of Tlemcen. This specific behavior may be attributed to the influence of the frequency content of the seismic motion and the geometry of structures on their dynamic responses. It should be noted that the distribution of critical zones, recorded under the earthquake of Boumerdès, is similar to that observed under the earthquake of Tlemcen. The stress concentrations, as well as the plastic deformation zones, appear in the same areas, but with a significantly larger extension under the earthquake of Boumerdès. This convergence of results clearly demonstrates that the Boumerdès earthquake does not modify the vulnerability mechanisms but simply amplifies their magnitude.

The maximum stress, strain, and displacement values obtained for the different structures are summarized in Tab. 13, which clearly depicts the differences between the two excitations and confirms the structures' sensitivity to the magnitude and frequency content of the motion.

Structures	$\sigma_{c,max}$ (MPa)		$\sigma_{T,max}$ (MPa)		$\sigma_{eq,max}^{DP}$		Max. displacement (cm)		$\varepsilon_{eq,max}^{p}$	
	X Axis	Y Axis	X Axis	Y Axis	X Axis	Y Axis	X Axis	Y Axis	X Axis	Y Axis
Structure 01	1.23	0.663	0.506	0.4483	0.485	0.4487	12.4	4.68	0.0106	0.000923
Structure 02	0.648	1.4	0.440	0.432	0.438	0.424	2.98	7	0.00109	0.00663
Structure 03	0.653	1.4	0.406	0.435	0.412	0.429	3.28	10.42	0.000765	0.00448
Structure 04	1.33	1.32	0.461	0.450	0.449	0.439	10.17	10.44	0.003538	0.00421
Structure 05	0.631	1.15	0.399	0.522	0.404	0.537	3.45	13.33	0.00145	0.00965
Structure 06	0.895	1.24	0.429	0.416	0.425	0.422	5.04	4.82	0.00238	0.00248

Table 13: Maximum mechanical response values of the six configurations subjected to Boumerdès earthquake.

Comparative Analysis of Seismic Responses of Structures Subjected to Tlemcen and Boumerdès Signals

The cross-analysis of all structural responses, using two accelerograms, shows a consistent distribution of critical zones, thus confirming that geometry is the dominant criterion in force distribution and damage accumulation.

It is worth mentioning that the sensitive zones are located mainly at the base of the intermediate walls, at the ends of free walls, and at the thickness transition zones in the tower walls, at a height of 8 m. However, it was observed that the magnitude of responses varies significantly depending on the signal applied. It is also to be noted that the earthquake of Boumerdès, which is characterized by a higher peak acceleration (5.02 m/s²) than that of Tlemcen (3.4 m/s²), induced a generalized increase in seismic response exceedances. However, some configurations, particularly Structure 05, exhibit slightly higher local responses under the Tlemcen excitation, as shown in Tab. 9 and 10 and in Fig. 51. This behavior is attributed to the interaction between the frequency content of the seismic motion and the inherent geometry of structures. This interaction influences ~~on~~ the dynamic responses of structures. Moreover, while the seismic vulnerability ranking remains unchanged (Structure 05 > 04 > 01 > 03 > 02 > 06), the earthquake of Boumerdès nevertheless reveals that the damage mechanisms get worse. This underlines the urgency of undertaking differentiated interventions and the need to adopt strengthening strategies that are suitable for each configuration. Furthermore, the Structures 05 and 04, which were identified as the most vulnerable, attained critical levels necessitating priority strengthening. As for the Structure 01, it exhibits intermediate behavior with notable exceedances but presents better relative strength. In contrast, the Structures 02, 03 and 06 show rather moderate responses, which means the possible occurrence of localized cracks, but without immediate risk of global instability.

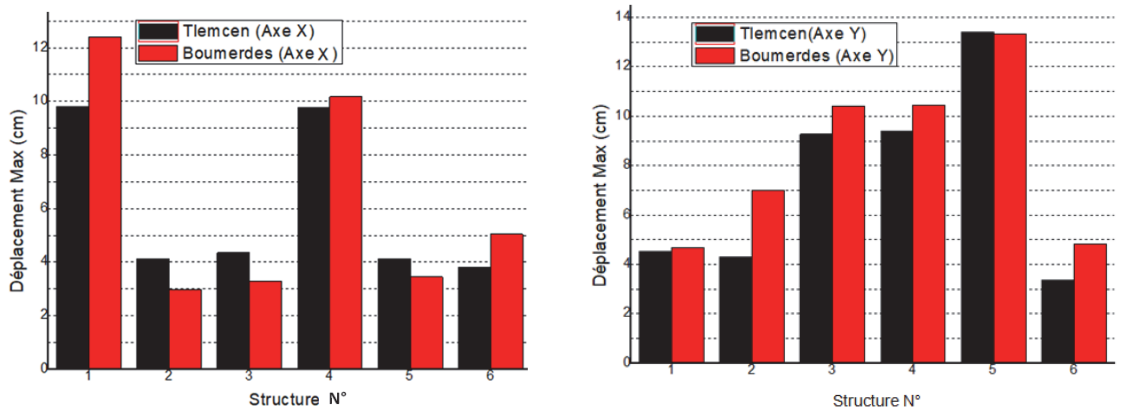

(a) (b)

Figure 51: Maximum displacements for all six geometric configurations (a) Along direction X, (b) Along direction Y.

CONCLUSION

The study presented in this work focused on six structural geometric configurations representative of the historical remains of the RE wall of Mansourah (Tlemcen, Algeria). These configurations were modeled with an elastoplastic behavior based on the Drucker–Prager criterion using ANSYS software. For this, two seismic excitations were applied. The first relates to concerns an artificial accelerogram derived from an elastic spectrum corresponding to the region of Tlemcen (3.52 m/s²) while the second relates to a real accelerogram that was recorded during the earthquake of Boumerdès (5.05 m/s²).

The dynamic response analysis of the structures was performed using the nonlinear time-domain method, while taking into account the directional variation of the seismic load along the horizontal X and Y axes. The results obtained were used to analyze the distribution of principal stresses (tension and compression), equivalent stresses, equivalent plastic strains, and to estimate maximum displacements. This made it possible to identify the areas of damage concentration. It is also to be noted that these critical zones are fairly consistent for the tow signals used. They are located primarily at the base of the intermediate walls, at the ends of free walls, and in the zones of thickness transitions of the walls constituting the towers, at an 8-meter height.

Furthermore, the comparative analysis shows that the Boumerdès earthquake, which was of higher magnitude than that of Tlemcen, generally induced higher maximum responses. However, it emerged that some configurations exhibited higher amplitudes under the excitation of the signal of Tlemcen for some specific physical quantities, demonstrating the combined influence of the signal frequency content and structural geometry on stress distribution and plastic deformation localization.

Finally, the seismic vulnerability classification, established from the overall responses, follows the descending order: Structure 05, 04, 01, 03, 02, 06. These findings confirm the relevance of the adopted numerical model and pave the way for reinforcement and rehabilitation approaches better suited to the dynamic specificities of historical RE monuments.

REFERENCES

[1] Avrami, E., Guillaud, H., Hardy, M. (2008). Terra literature review. An overview of research in earthen architecture conservation, Los Angeles, The Getty Conservation Institute.

[2] Bui, Q.B., Morel, J.C., Hans, S., Meunier, N. (2009). Compression behaviour of non-industrial materials in civil engineering by three scale experiments: the case of rammed earth, Materials and Structures, 42(8), pp. 1101–1116. DOI: https://doi.org/10.1617/s11527-008-9446-y.

[3] Soudani, L., Fabbri, A., Morel, J., Woloszyn, M., Chabriac, P.A., Wong, H., Grillet, A.C. (2016). Assessment of the validity of some common assumptions in hygrothermal modelling of earth based materials, Energy and Buildings, 1, pp. 498–511. DOI: https://doi.org/10.1016/j.enbuild.2016.01.025.

[4] Lilley, D.M., Robinson, J. (1995). Ultimate strength of rammed earth walls with openings, Proceedings of the Institution of Civil Engineers – Structures and Buildings, 110(3), pp. 278–287.

[5] Jaquin, P.A., Augarde, C.E., Gerrard, C.M. (2006). Analysis of Historic Rammed Earth construction, Structural Analysis of Historical Constructions, New Delhi, ISBN 972-8692-27-7.

[6] Maniatidis, V., Walker, P. (2008). Structural capacity of rammed earth in compression, Journal of Materials in Civil Engineering, 20(3), pp. 230–238. DOI: https://doi.org/10.1061/ (ASCE) 0899-1561(2008)20:3(230)

[7] Bui, Q.B., Morel, J.C., Reddy, B.V.V., Ghayad, W. (2009). Durability of rammed earth walls exposed for 20 years to natural weathering, Building and Environment, 44(5), pp. 912–919. DOI: 10.1016/j.buildenv.2008.07.001

[8] Bui, Q.B., Morel, J.C. (2009). Assessing the anisotropy of rammed earth, Construction and Building Materials, 23, pp. 3005–3011. DOI: https://doi.org/10.1016/j.conbuildmat.2009.04.011

[9] Bui, T.T., Bui, Q.B., Limam, A., Maximilien, S. (2014). Failure of rammed earth walls: From observations to quantifications, Construction and Building Materials, 51, pp. 295–302. DOI: https://doi.org/10.1016/j.conbuildmat.2013.10.053

[10] Bui, Q.B., Morel, J.C. (2015). First exploratory study on the ageing of rammed earth material, Materials, 8, pp. 1–15. DOI: https://doi.org/10.3390/ma8010001.

[11] Champiré, F., Fabbri, A., Morel, J.C., Wong, H., McGregor, F. (2016). Impact of relative humidity on the mechanical behavior of compacted earth as a building material, Construction and Building Materials, 110, pp. 70–78. DOI: https://doi.org/10.1016/j.conbuildmat.2016.01.027

[12] Arrigoni, A., Beckett, C., Ciancio, D., Dotelli, G. (2017). Life cycle analysis of environmental impact vs. durability of stabilised rammed earth, Construction and Building Materials, 142, pp. 128–136. DOI: https://doi.org/10.1016/j.conbuildmat.2017.03.066
[13] Bouhiyadi, S., Souinida, L., El Hassouani, Y. (2022). Failure analysis of compressed earth block using numerical plastic damage model, Frattura ed Integrità Strutturale, 62, pp. 634–659. DOI : https://doi.org/10.3221/IGF-ESIS.62.44
[14] Bui, Q.B., Limam, A., Bui, T.T. (2018). Dynamic discrete element modelling for seismic assessment of rammed earth walls, Engineering Structures, 175, pp. 690–699.
[15] Bui, Q.B., Hans, S., Morel, J.C., Do, A.P. (2011). First exploratory study on dynamic characteristics of rammed earth buildings, Engineering Structures, 33(12), pp. 3690–3695. DOI: https://doi.org/10.1016/j.engstruct.2011.08.004
[16] Gomes, M.I., Lopes, M., Brito, J. (2011). Seismic resistance of earth construction in Portugal, Engineering Structures, 33(3), pp 932-941. DOI: https://doi.org/10.1016/j.engstruct.2010.12.014
[17] Georgios, K., Lourenço, P.B. (2018). Structural assessment and seismic vulnerability of earthen historic structures. Application of sophisticated numerical and simple analytical models, Engineering Structures, 160, pp. 488–509. DOI: https://doi.org/10.1016/j.engstruct.2017.12.023
[18] Bui, Q.B., Tan-Trung, B., Mai-Phuong, T., Thi-Loan, B., Hoang-An, L. (2019). Assessing the Seismic Behavior of Rammed Earth Walls with an L-Form Cross-Section, Sustainability, 11, 1296. DOI: https://doi.org/10.3390/su11051296
[19] El-Nabouch, R., Bui, Q.B., Plé, O., Perrotin, P. (2017). Assessing the in-plane seismic performance of rammed earth walls by using horizontal loading tests, Engineering Structures, 145, pp. 153–161. DOI: https://doi.org/10.1016/j.engstruct.2017.05.027
[20] Nguyen, T.D., Bui, T.T., Ali, L., Thi-Loan, B., Bui, Q.B. (2021). Evaluation of seismic performance of rammed earth building and improvement solutions, Building Engineering, 43, pp. 103-113. DOI: https://doi.org/10.1016/j.jobe.2021.103113
[21] AFNOR. NF P 94-077 (1977). Uniaxial compression test.
[22] AFNOR. NF P 94-051 (1993). Soils: Determination of Atterberg limits – Liquid limit by Casagrande cup method and plastic limit by rolling method.
[23] AFNOR. NF P 94-064 (1993). Rocks: Determination of dry density of a rock specimen by hydrostatic weighing.
[24] AFNOR. NF P 94-048 (1996). Soils: Determination of calcium carbonate content ($CaCO_3$) by calcimeter method.
[25] AFNOR. NF P 94-068 (1998). Soils: Identification and testing – Determination of methylene blue adsorption capacity of a soil or rock material.
[26] AFNOR. NF EN 12390-6 (2010). Testing hardened concrete – Part 6: Tensile splitting strength.
[27] AFNOR. NF EN 12504-1 (2019). Testing concrete in structures – Part 1: Cored specimens – Taking, examining and testing in compression.
[28] Amade, P., Manh-Truong, N., Anh Minh, T. (2017). Un critère hyperbolique simple de résistance des roches, Geotechnique, 152, p.10. DOI: https://doi.org/10.1051/geotech/2017008
[29] Quoc-Bao, B. (2008). Stabilité des structures en pisé: durabilité, caractéristiques mécaniques, thèse de doctorat, Etablissement Lyon INSA.